LAWRENCE
LIVERMORE
NATIONAL
LABORATORY

LLNL-TR-816668

Quasi-stationary Planetary Scale Waves in Modern Climate Models

C. Covey, R. S. Lindzen, J. Fasullo, K. E. Taylor

November 11, 2020

Disclaimer

This work performed under the auspices of the U.S. Department of Energy by Lawrence Livermore National Laboratory under Contract DE-AC52-07NA27344.

Quasi-stationary Planetary Scale Waves in Modern Climate Models

CURT COVEY,[a] RICHARD S. LINDZEN,[b] JOHN FASULLO,[c] AND KARL E. TAYLOR[a]

[a] *PCMDI, Atmospheric, Earth and Energy Division, Lawrence Livermore National Laboratory, Livermore, California*

[b] *Earth, Atmospheric and Planetary Sciences Department, Massachusetts Institute of Technology, Cambridge, Massachusetts*

[c] *Climate Analysis Section, Climate and Global Dynamics Division, National Center for Atmospheric Research, Boulder, Colorado*

November 2020

LLNL-TR-816668

ABSTRACT

We evaluate climate model simulations of geopotential height at the largest space-time scales, considering the first Fourier components (in longitude) of long-term climatological means. Quasi-stationary planetary scale waves emerge from this analysis. Variations of these waves are important components of climate change, for example associated with regional drought. Systematic examination of their long-term climatology provides context for understanding their evolution in time. We compare four reanalysis datasets with "historical runs" from the latest version of the Coupled Model Intercomparison Project (CMIP) and find general agreement, but we also identify model errors outside the range of both observational uncertainty and the uncertainty implied by interannual variability. Errors in wave phase have possible implications for climate model projections of regional climate and of shifting weather patterns. One model in the set we examine, originally created nearly 20 years before the others, exhibits noticeably greater errors.

1. Introduction

The major contribution to atmospheric eddies of the largest horizontal scale—the same order as the planetary radius—is made by nearly stationary waves forced by flow over fixed features of Earth's surface and by thermal contrast near the surface (Smagorinsky 1953, Charney and Drazin 1961, Jacqmin and Lindzen 1985, Held et al. 2002, Nigam and DeWeaver 2015). In addition to being major components of the general circulation, crucially important for regional climate as well as stratospheric dynamics, they help guide transient weather systems (Niehaus, 1980) and interact with the ocean (particularly the Tropical Pacific) to generate modes of climate variability (Liu and Alexander 2007, Newman et al. 2016, Fasullo et al. 2020).

Many studies associate extreme weather events—including heat waves and droughts, and on other occasions severe storms—with a shifting climatology of quasi-stationary planetary scale waves in both the troposphere and the stratosphere, associated with anthropogenic global warming (e.g. Simpson et al. 2015, Mann et al. 2017, Kretschmer et al. 2018). Naturally forced climate changes, of course, can also involve these waves (e.g. Chen et al. 2020).

Global weather balloon observations during the 20th century allowed these waves to be mapped in the geopotential height field. Van Loon and Jenne (1972) and van Loon et al. (1973) evaluated their climatology by computing Fourier components in the zonal (longitude) direction and plotting their amplitude and phase as a function of latitude and altitude. This simple decomposition is particularly useful because nearly all of the spatial variance of monthly mean geopotential is contributed by the first three or four zonal wavenumbers (see below). Yet we can

find it applied to climate model evaluation in only one paper (Rind et al. 1988, Figs. 15-16)—and even in this study, geopotential height simulation was deemed satisfactory but not explored in detail.

Subsequently, the Coupled Model Intercomparison Project (CMIP) has accumulated climate model output and generated hundreds of papers, but few have dealt with the long-term climatology of atmospheric stationary waves. Boyle (2006) examined streamfunction (equivalent to geopotential if geostrophically balanced) at a single pressure level, 250 hPa. Instead of using Fourier analysis, Boyle (2006) computed spatial correlation coefficients between CMIP3 models and the ERA40 reanalysis "observations" (see below for a brief evaluation of reanalysis). He found values mainly upwards of ~0.5 and concluded that most prominent model errors diminished as model resolution increased up to about 2.5° in longitude and latitude. At finer resolutions, model accuracy was less dependent on grid spacing.

Subsequent work investigated how stationary waves might change with global warming but only briefly compared their long-term climatology with observations. Brandefelt et al. (2008) found a spatial pattern correlation between CMIP3 and ERA40 reanalysis in the range 0.69-0.96, similar to Boyle's work except that Brandefelt's data were averaged vertically within the troposphere. Simpson et al. (2015) noted that at the 300 hPa level, "climatological wave amplitude in the observationally based reanalysis lies at the low end of the modelled range" from CMIP5. A recent review of Northern Hemisphere stationary waves presents two figures comparing CMIP5 control simulations with ERA-I reanalysis before commencing an extensive discussion of how these waves might change in the future; it reaches two qualitative conclusions: "The CMIP5

multi-model mean reproduces the observed winter stationary wave climatology remarkably well," while for summer, "good agreement" with observations obtains at the largest scales but "there remains poor agreement between models on present-day climatologies at the regional scale" (Wills et al. 2019).

Some time ago, one of us wrote in a review entitled "Stationary Planetary Waves, Blocking, and Interannual Variability" (Lindzen 1986): "It seems to me that much of the current approach is unbalanced at best. Far more work is being devoted to accounting for anomalies than to accounting for the climatology itself." Since that time the imbalance has continued, as noted above. A focus on model-simulated climatology is overdue in our opinion. It is particularly warranted for quasi-stationary waves because singularities appear in the differential equations governing first-order dynamics when the mean zonal wind vanishes, generating discontinuities in their solutions (Dickinson 1968, Section 4). In these circumstances, discrete numerical approximations may become problematic.

2. Data sources and data processing

Fourier analysis is particularly suited for inter-comparison of a large number of climate models, condensing much data into relatively concise metrics. Here we apply this diagnostic to simulations from the latest version of CMIP (CMIP6) together with corresponding observations.

Table 1 shows our data sources for both observations and climate model output. Following the recommendation of Abramowitz et al. (2019), we select one coupled (ocean + atmosphere + land

+ seaice) model from each CMIP6 modeling institution. Although this procedure is a crude approach to finding "independent" models, it provides a diverse yet tractable number of models: 18 in our case. One model we selected—MCM-UA-1-0, currently maintained at the University of Arizona—is a copy of the 1991 Manabe Climate Model developed at NOAA-GFDL. All other models represent the current state of the climate-modeling art. Inclusion of MCM-UA-1-0 allows comparison of a much older, lower resolution model with the modern set.

For observations, we use products of the four latest global reanalysis projects. Reanalysis employs a numerical weather prediction model to process observations (as if initializing a weather forecast), thereby giving a self-consistent set of meteorological fields. Use of reanalysis output follows Boyle (2006) and many others but raises a question: Are we comparing models with other models, rather than comparing models with actual observations? This problem may occur for fields that are computed by the reanalysis model using only observations of different fields, e.g. if the model computes surface energy fluxes from observed near-surface temperature and wind fields, but does not include any observed fluxes. Fortunately, direct assimilation of geopotential height data occurs densely in space-time for satellite era reanalyses (post-1979). Thus reanalysis of geopotential height is more like interpolation constrained by well-known physical principles (Kalnay et al. 1996). The well-constrained nature of geopotential height in both hemispheres arises mainly from data provided from the TIROS Operational Vertical Sounder (TOVS) aboard polar orbiting satellites, which observe tropospheric temperature (Jun et al. 1994). The sampling provided by TOVS has been twice daily during most of our analysis period.

To confirm this well-constrained character, Figs. 1-5 compare a sample of geopotential height data from reanalysis with direct compilations of weather balloon observations. The latter were published in the early days of global meteorology and are not widely available for recent years. Accordingly, for global weather balloon observations *not* constrained by models, we use an early published dataset from Palmen and Newton (1969) and compare it with the one reanalysis dataset that is available for a corresponding period, JRA-55. Figures 1-5 show the results together with reanalysis data from more recent years and from a second reanalysis project. Unfortunately, Palmen and Newton's data is available only as printed contour maps, so quantitative comparison with other data is not possible; but a visual inspection of Figs. 1-5 reveals very little difference between the various datasets. We conclude that for large scale climatology of quasi-stationary waves, reanalysis can indeed be equated with observations. Additionally, from Figs. 1-5 it seems that for large space-time scales there is very little difference between the second half of the 20th century and more recent times, or between different reanalysis datasets.

All geopotential heights studied here are publicly available. CMIP6 output is at https://esgf-node.llnl.gov/projects/cmip6/. ERA5 data is obtained from the Copernicus Climate Change Service (C3S) Climate Date Store (https://cds.climate.copernicus.eu) and our other reanalysis data is from Ana4MIPs (Gleckler et al. 2014; https://earthsystemcog.org/search/obs4mips/). These different reanalysis datasets overlap for the period 1990-2013, so we choose this period to compare the reanalyses with climate model simulations. Note that CMIP6 historical simulations cover the period 1850–2014 (Eyring et al. 2016).

All data are reduced to January and July climatological means for 1990-2013, then processed by Fourier transform in the longitude (λ) dimension:

$$f(\lambda) = C_0 + \sum_{n=1}^{\infty} C_n \cos[n(\lambda - \lambda_n^{MAX})] = C_0 + \sum_{n=1}^{\infty} a_n \cos(n\lambda) + b_n \sin(n\lambda). \quad (1)$$

The coefficient C_0 is the zonal mean shown in Fig. 1. The constants C_n and λ_n^{MAX} ($n = 1, 2, 3, ...$) give the amplitude and phase, respectively, of the n^{th} Fourier component, with λ_n^{MAX} specifying the longitude of the "first" ridge in geopotential. Coefficients a_n and b_n in the second equality are determined by the inversion formulas

$$a_n = \frac{1}{\pi}\int_0^{2\pi} f(\lambda)\cos(n\lambda)\, d\lambda; \qquad b_n = \frac{1}{\pi}\int_0^{2\pi} f(\lambda)\sin(n\lambda)\, d\lambda \quad (2)$$

at each point in latitude / altitude space, and for each zonal wavenumber *n.* Standard trigonometric identities applied to Equation (1) then give C_n and λ_n^{MAX}, and the components of total variance are given by

$$\frac{1}{2\pi}\int_0^{2\pi}[f(\lambda) - C_0]^2\, d\lambda = \frac{1}{2}\sum_{n=1}^{\infty} {a_n}^2 + {b_n}^2. \quad (3)$$

We have computed Fourier components for wavenumbers $n = 1$ to 5. These these include more than 80% of total variance at nearly all points in latitude / altitude space; after integrating vertically, the first four wavenumbers include more than 80% of variance at all latitudes (Figs. S1-S2).

3. Results

a. Selected climate models in detail

Van Loon and Jenne (1972) and van Loon et al. (1973) took data from only one source: radiosonde observations. [Figure captions in their papers cite I. Jacobs (1958) for Northern Hemisphere data and Taljaard et al. (1969) for Southern Hemisphere data; the cited work, in turn, points to "gray literature" reports from the Free University of Berlin and the US Navy.] Applying Fourier analysis, van Loon and colleagues displayed and discussed a total of eight contour maps of C_n and λ_n^{MAX} as functions of latitude and altitude. Here we deal with too many data sources to inspect one van Loon-type contour map for both amplitude and phase of each. We are therefore selective in displaying contour maps, turning to more concise statistics in the next subsection for the full set of data sources. For contour maps, we select the latest reanalysis (ERA5) together with the three climate models with longest pedigrees: CESM2 from the National Center for Atmospheric Research, GFDL-CM4 from the NOAA Geophysical Fluid Dynamics Laboratory, and GISS-E2-1-G from the NASA Goddard Institute for Space Studies.

Figure 6 shows the Fourier amplitude of January climatological means for the first three zonal wavenumbers. The vertical coordinate is pressure, expressed as altitude in scale heights: $z \,/\, H = \ln\,(p_{surface} \,/\, p)$. For later reference, the 850 hPa, 500hPa and 200 hPa pressure levels are marked by horizontal dashed lines, and 45°S and 45°N latitudes are marked by vertical dashed lines. The three climate model simulations give results quite similar to ERA5—and also in agreement with observations shown by van Loon and colleagues. For example, Van Loon and

Jenne (1972) note that in January in the Southern Hemisphere, maximum wave 1 amplitude is ~100 m at ~50-60°S latitude and ~1 scale height altitude. For the Northern Hemisphere in January, van Loon et al. (1973) say "The highest values of wave 1 in the troposphere [i.e. below the 200 mb pressure level] occur between 45° and 50°N" at 1-2 scale heights; also "The peak [amplitude] in the stratosphere is 20° of latitude poleward of the one in the troposphere." These features are evident in all the top-row frames on Fig. 6.

For wavenumber 2, the middle-row frames in Fig. 6—both reanalysis and model simulations—agree with van Loon et al. (1973) in that "The peak amplitude of wave 2 stays in nearly the same latitude (60°N) in most of the troposphere and part of the stratosphere." Wavenumber 3 (lower frames) in contrast to waves 1-2 weakens in the stratosphere in both reanalysis and model simulations. Suppression of wavenumbers $\gtrsim 2$ is a fundamental feature of wave propagation from the troposphere to the stratosphere (Charney and Drazin 1961). It can be understood in terms of an "equivalent depth" (related to refractive index) that changes from positive to negative values, passing through a singularity, as wavenumber increases (Lindzen 1990, Section 11.2). Van Loon et al. (1973) also noted this feature: "The third trough in the tropospheric mean circulation . . . to which wave 3 owes its large amplitude, weakens quickly in the lower stratosphere, and wave 3 accordingly decays in the stratosphere."

On the other hand, discrepancies with reanalysis in Fig. 6 are readily seen. GFDL-CM4 underestimates the polar stratosphere's wave 1 amplitude, while GISS-E1-G generally underestimates wave 3 amplitude. The maximum amplitude of wave 3 exceeds 100 meters in the midlatitude upper troposphere in CESM2 and GFDL-CM4 simulations, in agreement not only

with reanalysis but also with earlier direct observations of van Loon et al. (1973, their Fig. 4); GISS-E1-G places the maximum correctly but underestimates its magnitude by a factor of two. In the Southern Hemisphere, all three models place maximum wavenumber 3 amplitude correctly, but CESM2 *over*estimates it by a factor of two.

Figure 7 shows contours of January Fourier phase, corresponding to the amplitude contour maps in Fig. 6. Phase is defined as the longitude of the first maximum of geopotential, i.e. the first ridge as one looks eastward from the zero meridian. The phase plots are more difficult to interpret than amplitude plots as isolines of phase can become jumbled, mainly because phase is poorly defined for small amplitudes. Nevertheless, substantial similarity between any two pairs of data sources is evident. For waves 1 and 3 at least, the most prominent feature in both reanalysis and models is a set of parallel vertical lines in the middle latitudes of both hemispheres (in the vicinity of 45°S and 30°N) running upward from about the 850 hPa pressure level. These lines indicate a phase reversal from about +120° to –120° longitude as one goes poleward from the tropics into middle latitudes.

To provide more quantitative comparisons, Table 2 gives amplitude and phase numbers at six sample points in latitude / altitude space where the horizontal and vertical dashed lines in Figs. 6-7 meet, i.e. at the 850-, 500- and 200-hPa pressure levels and ±45° latitude. The table adds to ERA5 the products of the three earlier reanalysis projects, revealing extremely close agreement at nearly all of the sample points. It also includes wave 4, showing that Fourier amplitudes begin to decline at higher wavenumbers. The decline continues for waves 5-6 (*not shown*). Wavenumbers larger than 6 are associated more with traveling waves than with quasi-stationary waves (Wallace and Hobbs 2006, p. 14) and are not included in this study.

Many of the discrepancies between climate models and reanalysis noted above may be seen in Table 2. For example, GISS-E1-G's underestimate of wave 3 amplitude in the upper troposphere amounts to a factor of two difference from reanalysis at $p = 200$ hPa and 45°N. GFDL-CM4's equally severe underestimate of wave 1 amplitude in the middle stratosphere ($z\ /\ H \sim 3$) and 65°N is not included our sample points, but it is reflected in this amplitude's 20% shortfall at $p = 200$ hPa and 45°N. Other model shortcomings that are quantified in Table 2 include CESM2's severe underestimates of wave 2 amplitude at 45°S latitude and $p = 500$ and 200 hPa, and a large scatter of wave 1 phases among all three climate models. For example, at 45°N and 500 hPa, the wave 1 phase (i.e. the longitude of the ridge) varies only between 15°W and 17°W in the three reanalyses, but it varies between 26°W and 3°E in the three climate models. The difference between the models persists when an ensemble of runs with varying initial conditions is examined, implying that the scatter reflects inherent model errors rather than internal variability (Fig. S3).

Turning to the month of July, Figs. 8 and 9 show contour maps of amplitude and phase, respectively, and Table 3 gives corresponding numbers at sample points (analogous to the January climatology data in Figs. 6-7 and Table 2). As in January, the July data exhibit substantial agreement between reanalysis and climate models but also some discrepancies. For example, all three of our selected climate models get overly large wave 3 amplitudes in the Southern Hemisphere compared with both ERA5 data (Fig. 8) and earlier direct observations (van Loon and Jenne 1972, their Fig. 7). Table 3 shows that the extent of overestimate ranges from 15% to 60% at 45°S and $p = 850$, 500 and 200 hPa. The phase contour maps for July (Fig. 9), as with January, are more difficult to interpret than the amplitude contour maps but show an obvious correlation between any of our three selected climate models and ERA5. Likewise, the

phase values at nearly all sample points in Table 3 reveal close agreement between reanalysis projects but considerable scatter among the climate models.

One issue arising in any comparison of climate models with observations is how robust the results may be with respect to interannual variability. Although output from CMIP historical runs is identified with particular calendar years (in our case 1990-2013) no attempts were made in these simulations to initialize them at the correct phase of variations like El Nino / La Nina. Even if the runs been initialized in that way, chaotic effects would make a precise year-by-year comparison with observations inappropriate. Does the resulting uncertainty mean that the model / reanalysis discrepancies identified above lie within "error bars" implied by interannual variability? This hypothesis is not supported by an ensemble of 10 runs each from CESM2 and GISS-E1-G, with initialization from various time points in a long steady-state climate simulation (see Figs. S3-S4; analogous ensemble runs are not available from GFDL-CM4). As noted above in connection with Table 2, the CESM2 and GISS-E1-G ensembles form two distinct groups that seldom overlap. Further, as shown in Figs. 2-5, the overall appearance of the waves is not changed by using the 1990-2013 reanalysis or much earlier data for observations.

b. All CMIP6 models at selected pressure levels

Figures 10 and 11 show wavenumber 1-3 Fourier amplitude and phase, respectively, at our canonical three pressure levels for January climatological means. Figures 12 and 13 show the same for July climatological means. These figures are in effect horizontal slices through Figs. 6-9. However, they include results from all 18 available CMIP6 models, and either all four

reanalyses (top two rows) or ERA5 reanalysis both as given and as extrapolated per the Appendix (bottom rows) Selecting one pressure level allows results from all data sources to appear in a single line plot of amplitude or phase as a function of latitude.

Figures 10-13 each show results from three pressure levels: 200 hPa near the bottom of the stratosphere, 500 hPa in the mid-troposphere, and 850 hPa nearer the surface. The 200 hPa level reveals planetary scale waves more clearly than in the troposphere because baroclinic waves are suppressed in the more stable stratosphere. The "steering level" at which quasi-stationary planetary scale waves guide smaller scale weather systems is ~700 hPa (Wallace and Hobbs 2006, Section 8.3—in between our two lower levels.

The 850 hPa level comes closest to the weather that most people experience, but it presents a problem: geopotential height at this level is undefined in numerous cases where the actual surface pressure is less than 850 hPa. Numerical weather prediction algorithms routinely avoid this inconvenience by applying hydrostatic balance to a fictitious below-ground atmosphere, thereby deducing 850 hPa geopotential heights below the surface. The algorithms vary between different models and entail fairly arbitrary assumptions. Accordingly, we apply one simplified procedure to all of our data sources in order to make the 850 hPa pressure surface continuous along most latitude circles, omitting only latitude bands that encompass Greenland, the Himalayas, and the Antarctic plateau (see Appendix). For the included latitudes, our procedure gives nearly the same results as ECMWF's own procedure (compare solid vs. dashed lines in the bottom rows of Figs. 10-13).

Figures 10 and 12 show that at 850 hPa and 500 hPa, most models agree with reanalysis to within ±20% in their simulation of Fourier amplitudes at nearly all latitudes. But examining results from a higher altitude, $p = 200$ hPa, reveals more serious discrepancies. At this level, many model simulations disagree with reanalysis amplitudes by a factor of two or more at several latitudes. This disagreement is particularly noticeable for the 1991 "Manabe Climate Model" MCM-ESM2-0, which has the lowest model top of our model set; like most models of its vintage, this model focused on the troposphere at the expense of the stratosphere. Phase data (Figs. 11 and 13) are in some ways more problematic than the amplitude data at all levels, e.g. a systematic disagreement with reanalysis seems to arise in all models equatorward of ~30° latitude (although wave amplitude is weak here, and the phase correspondingly less meaningful). Nevertheless, it is clear from the Figs. 10-13 that all 18 CMIP6 models exhibit the same general patterns of reanalysis amplitude and phase that are evident for the three selected models in Figs. 6-9.

Despite this general agreement between climate models and observations, the spread of model results in Figs. 10-13 is clearly greater than the spread of reanalysis results and very much greater than the spread of ensemble members for either of the models running with different initial conditions (Figs. S3-S4), making it difficult to deny that most model simulations lie outside observational "error bars." At the 500 hPa and 200 hPa levels, the four reanalysis data sets overlay each other so closely as to be indistinguishable at all but a few latitudes. (Data limitations precluded extrapolation of any but ERA5 reanalysis to 850 hPa.) This concordance is also evident in the sample points of Tables 2-3. As discussed above, in the case of geopotential height the reanalysis procedure is more about interpolating the observations than producing a

model-simulated outcome. Thus, at the low space-time resolution of our study, the observations provide a strong constraint on models. Any model biases should be taken seriously.

4. Discussion

Like many parts of science, atmospheric general circulation models deal with an extremely complex physical system. Adding other components of the climate system only increases the complexity. Consequently, "all [climate] models are wrong" and "the practical question is how wrong do they have to be to not be useful" (Box and Draper 1987). The answer to this question, of course, depends on what the model is used for.

When connecting weather patterns with the climatology of long atmospheric waves, the model accuracy required for usefulness can be fairly high. For example, a shift of only a few degrees longitude in the mid-tropospheric ridge associated with California's recent severe drought (Swain et al. 2014, Fig. 2.1g) would create a very different regional climate. Figure 13 shows that different CMIP6 models simulate widely differing July phase at any one latitude. The typical range is of order tens of degrees in longitude. A phase error of a few degrees in one Fourier component may potentially be canceled by errors in other components, and such cancellation might reflect a physical constraint that ensures flow through California in the correct direction even if flows due to individual stationary waves are problematic—but the model spread in phase plots at least warrants serious attention. For example, a clear implication of the early studies of Smagorinsky (1953) and Charney and Drazin (1961) is that simulation of stationary waves depends on the correct specification of orographic and thermal forcing. Dependence on the zonal

mean flow is also critical (Nigam and Lindzen 1989). Simultaneous examination of these factors as well as stationary waves may help lead to more accurate simulations.

The work presented here only begins an assessment of quasi-stationary planetary scale waves simulated by CMIP6 models. The absence of clear "outliers" among the models (with the possible exception of the older, low-resolution MCM-UA-1-0) is consistent with Boyle's 2006 suggestion that with sufficiently high horizontal resolution, simulations of the waves reach a plateau of accuracy. It remains to be determined whether that level of accuracy suffices to draw firm connections between the longest space-time scales of atmospheric dynamics and the weather events of immediate relevance to humanity.

Acknowledgments. We thank Prof. Gerald Schubert for useful comments. Work was performed under auspices of the Regional and Global Model Analysis Program, DOE Office of Science by Lawrence Livermore National Laboratory under Contract DE-AC52- 07NA27344 (for KET), and at the National Center for Atmospheric Research, which is sponsored by the US National Science Foundation (for JF). Computing resources (doi:10.5065/D6RX99HX) were provided by the Climate Simulation Laboratory at NCAR's Computational and Information Systems Laboratory, sponsored by NSF and other agencies. We acknowledge the World Climate Research Programme and its Working Group on Coupled Modelling, which coordinated and promoted CMIP6. We thank the climate modeling groups for producing and making available their model output, the Earth System Grid Federation (ESGF) for archiving the data and providing access, and the multiple funding agencies who support CMIP and ESGF.

APPENDIX: **Infilling Geopotential Height at 850 hPa**

a. Theoretical formulation

Geopotential height Z_p at pressure level p is not well defined for elevated terrain where the surface pressure $p_{sfc} < p$. One must imagine the p-level extending below the surface, so that Z_p is less than surface elevation Z_{sfc}. Invoking hydrostatic equilibrium below the surface (!) then implies

$$Z_{sfc} - Z_p = \overline{H} \ln(p / p_{sfc})$$

where $\overline{H}$ is the average scale height $R\,\overline{T^*}/g$ in a fictitious atmospheric layer below the surface. T^* is that layer's virtual temperature:

$$T^* = \frac{T}{1 - (e/p)\,(1 - M_w/M_d)},$$

e is water-vapor pressure, and $M_w/M_d \approx 0.622$ is the ratio of molecular weights of water and dry air (e.g. Chapter 3 in Wallace and Hobbs 2006). Often this procedure is used to reduce data to sea level where $p \approx 1013$ hPa. For our study we need only go down to $p = 850$ hPa.

What is a reasonable extrapolation of T^* below the surface? Describing the standard procedure, Pauley (1998) says that "Commonly, $\overline{T^*}$ is approximated as the average of some surface virtual temperature T^*_{sfc} and a [below-surface] virtual temperature . . . that is obtained by extrapolating T^*_{sfc} downward using a constant virtual lapse rate γ^*. . . set equal to the standard atmospheric lapse rate, γ_s, equal to 6.5 K / km." Thus

$$\overline{T^*} = \frac{T^*_{sfc} + T^*_p}{2} = \frac{2\,T^*_{sfc} + \gamma^*(Z_{sfc} - Z_p)}{2}$$

Combining the equations above gives a linear equation in $Z_{sfc} - Z_p$, with solution

$$Z_{sfc} - Z_p = \frac{(R\,T^*_{sfc}/g)\;\ln(p/p_{sfc})}{1 - (\gamma^* R/2g)\;\ln(p/p_{sfc})}$$

In the above equation, extrapolation below the surface is done using only two-dimensional fields defined at (or near) the surface: terrain elevation Z_{sfc}, temperature T_{sfc}, pressure p_{sfc}, and humidity (which gives virtual temperature T^*_{sfc} via e_{sfc}).

Pauley notes that the US National Weather Service uses a more complicated formulation, including an empirical "humidity correction" and additional corrections that bring γ^* closer to the actual lapse rate. She also advocates "defining the below-ground temperature field by horizontal interpolation across terrain features" as an additional step. We do not consider these refinements necessary for our current study, as long as a few latitudes are omitted from the data processing. This conclusion is based on the following test case.

b. ERA5 data as a test case

ERA5 reanalysis data provided by the European Center for Medium-range Weather Forecasting includes Z_p values where $p_{sfc} < p$. This allows us to test our procedure using ERA5 surface data in the above equations, comparing the resulting $Z_{850\,hPa}$ field with the original ERA5 field. Figure A1 maps these fields in latitude-longitude space for climatological January and July of our standard time period, 1990-2013. Problematic features appear both in the original ERA5 field and in our version, though of course the more sophisticated ECMWF extrapolation procedure gives better-looking results. Most notable are discontinuities around the highest terrain (especially the Himalayas) that are more severe in our version. In addition, close inspection reveals a faint imprint of continental outlines in both versions--evidently another unphysical discontinuity.

Figure A2 shows the Fourier amplitude and phase of the fields in Fig. A1 for zonal wavenumbers 1-4. The different wavenumbers are color-coded as indicated in the figure. Comparison of original ERA5 data (*light colors)* with our version (*dark colors*) reveals good agreement except for the following latitude bands, which are shaded in gray in the figure: 90 °S < ϕ < 70 °S (south polar region including the Antarctic Plateau), 75 °N < ϕ < 90 °N (north polar region including Greenland), and 25 °N < ϕ < 40 °N (the latitude band including the Himalayas). Accordingly, we will treat 850 hPa data from these regions as "missing" in the current study.

REFERENCES

Box, G. E. P., and N. R. Draper, 1987: p. 74 in *Empirical Model-building and Response Surfaces*, Wiley, 669 pp.

Boyle, J. S., 2006: Upper level atmospheric stationary waves in the twentieth century climate of the Intergovernmental Panel on Climate Change simulations. *J. Geophys. Res. Atmos.*, **111**, D14, https://doi.org/10.1029/2005JD006612.

Boucher O., and 78 co-authors, 2020: Presentation and evaluation of the IPSL-CM6A-LR climate model. *Journal of Advances in Modeling Earth Syste*ms, **12**, e2019MS002010. https://doi.org/ 10.1029/2019MS002010.

Brient, F., R. Roehrig, and A. Voldoire, 2019: Evaluating marine stratocumulus clouds in the CNRM-CM6-1 model using short-term hindcasts. *Journal of Advances in Modeling Earth Systems*, **11**, 127-148, https://doi.org/10.1029/2018MS001461.

Charney, J. G., and P. G. Drazin, 1961: Propagation of planetary-scale disturbances from the lower into the upper atmosphere. *J. Geophys. Res.*, **66**, 83-109, DOI: 10.1029/JZ066i001p00083.

Chen, K., and 10 co-authors, 2020: One drought and one volcanic eruption influenced the history of China: The late Ming Dynasty mega-drought. *Geophys. Res. Lett.*, **47**, e2020GL088124. https://doi.org/10.1029/2020GL088124.

Counillon, F., N. Keenlyside, I. Bethke, Y. Wang, S. Billeau, M. L. Shen, and M. Bentsen, 2016: Flow-dependent assimilation of sea surface temperature in isopycnal coordinates with the Norwegian Climate Prediction Model. *Tellus A: Dynamic Meteorology and Oceanography*, **68**:1, 32437, DOI: 10.3402/tellusa.v68.3243.

Danabasoglu, G., and 42 co-authors, 2020: The Community Earth System Model Version 2 (CESM2). *Journal of Advances in Modeling Earth Systems*, **12**, e2019MS001916, https://doi.org/10.1029/2019MS001916.

Dee, D. P., and 36 co-authors, 2011: The ERA-Interim reanalysis: configuration and performance of the data assimilation system. *Quarterly Journal of the Royal Meteorological Society*, **137**, 553-597, https://doi.org/10.1002/qj.828.

Delworth, T., R. Stouffer, K. Dixon, M. Spelman, T. Knutson, A. Broccoli, P. Kushner, and R. Wetherald, 2002: Review of simulations of climate variability and change with the GFDL R30 coupled climate model. *Climate Dynamics*, **19**, 555-574, DOI:10.1007/s00382-002-0249-5

Dickinson, R. E., 1968: Planetary rossby waves propagating vertically through weak westerly wind wave guides. *J. Atmos. Sci.*, **25**, 984–1002, https://doi.org/10.1175/1520-0469(1968)025<0984:PRWPVT>2.0.CO;2.

Eyring, V., S. Bony, G. A. Meehl. C. A. Senior, B. Stevens, R. J. Stouffer, and K. E. Taylor, 2016: Overview of the Coupled Model Intercomparison Project Phase 6 (CMIP6) experimental design and organization. *Geosci. Model Dev.*, **9**, 1937-1958, DOI: 10.5194/gmd-9-1937-2016.

Fasullo, J. T., A.S. Phillips, and C. Deser, 2020. Evaluation of Leading Modes of Climate Variability in the CMIP Archives. *Journal of Climate*, **33**(13), 5527-5545.

Gelaro, R., and 30 co-authors, 2017: The Modern-Era Retrospective Analysis for Research and Applications, Version 2 (MERRA-2). *J. Climate*, **30**, 5419–5454, https://doi.org/10.1175/JCLI-D-16-0758.1.

Golaz, J.-C., and 85 co-authors, 2019: The DOE E3SM coupled model version 1: Overview and evaluation at standard resolution. *Journal of Advances in Modeling Earth Systems*, **11**, 2089-2129, https://doi. org/10.1029/2018MS001603.

Guo, C., M. Bentsen, I. Bethke, M. Ilicak, J. Tjiputra, T. Toniazzo, J. Schwinger, and O. H. Otterå, 2019: Description and evaluation of NorESM1-F: a fast version of the Norwegian Earth System Model (NorESM). *Geosci. Model Dev*., **12**, 343-362, https://doi.org/10.5194/gmd-12-343-2019.

Held, I. M., M. Ting, and H. Wang, 2002: Northern Hemisphere stationary waves: Theory and modeling, *J. Climate*, **15**, 2125-2144, https://doi.org/10.1175/1520-0442(2002)015<2125:NWSWTA>2.0.CO;2.

Held, I. M., and 44 co-authors, 2019: Structure and performance of GFDL's CM4.0 climate model. *Journal of Advances in Modeling Earth Systems*, **11**, 3691- 3727, https://doi.org/10.1029/2019MS001829.

Hersbach, H., and 42 co-authors, 2020: The ERA5 global reanalysis. *Quarterly Journal of the Royal Meteorological Society*, **146**, 1999-2049, https://doi.org/10.1002/qj.3803.

Jacqmin, D., and R. S. Lindzen, 1985: The causation and sensitivity of northern planetary waves, *J. Atmos. Sci.*, **42**, 724-745.

Jun, L., Z. Fengxian., and Z. Qingcun, 1994: Simultaneous non-linear retrieval of atmospheric temperature and absorbing constituent profiles from satellite infrared sounder radiances. *Advances in Atmospheric Sciences*, **11**, 128-138.

Kelley, M., and 45 co-authors, 2020: GISS-E2.1: Configurations and Climatology. *Journal of Advances in Modeling Earth Systems*, **12**, e2019MS002025. https://doi.org/10.1029/2019MS002025.

Kobayashi, S., and 11 co-authors, 2015: The JRA-55 Reanalysis: General specifications and basic characteristics, *J. Meteorological Society of Japan*, **93**, 5-48, DOI:10.2151/jmsj.2015-001.

Kornhuber, K., S. Osprey, D. Coumou, S. Petri, S. Rahmstorf, and L. Gray, 2019: Extreme weather events in early summer 2018 connected by a recurrent hemispheric wave-7 pattern. *Env. Res. Lett.*, **14**, 054002, https://doi.org/10.1088/1748-9326/ab13bf.

Kretschmer, M., D. Coumou, L. Agel, M. Barlow, E. Tziperman, and J. Cohen, 2018: More-persistent weak stratospheric polar vortex states linked to cold extremes. *Bull. Amer. Meteor. Soc.*, **99**, 49-60, https://journals.ametsoc.org/doi/abs/10.1175/BAMS-D-16-0259.1.

Lindzen, R. S., 1986: Stationary planetary waves, blocking, and interannual variability. *Advances Geophys.*, **29**, 251-273.

Liu, Z., and M. Alexander, 2007: Atmospheric bridge, oceanic tunnel, and global climatic teleconnections. *Reviews Geophys.*, **45**, RG2005, https://doi.org/10.1029/2005RG000172.

Mann, M. E., S. Rahmstorf, K. Kornhuber, B. A. Steinman, S. K. Miller, and D. Coumou, 2017: Influence of anthropogenic climate change on planetary wave resonance and extreme weather events. *Scientific Reports*, **7**, Article Number 45242, https://www.nature.com/articles/srep45242.

Massonnet, F., M. Ménégoz, M. Acosta, X. Yepes-Arbós, E. Exarchou, and F. J. Doblas-Reyes, 2020: Replicability of the EC-Earth3 Earth system model under a change in computing environment. *Geosci. Model Dev.*, **13**, 1165-1178, https://doi.org/10.5194/gmd-13-1165-2020

Newman, M., and Coauthors, 2016: The Pacific decadal oscillation, revisited. J. Climate, 29, 4399–4427, https://doi.org/10.1175/ JCLI-D-15-0508.1.

Niehaus, M., 1980: Instability of non-zonal baroclinic flows. *J. Atmos. Sci.*, **37**, 1447-1463, https://doi.org/10.1175/1520-0469(1980)037<1447:IONZBF>2.0.CO;2.

Nigam, S., and E. DeWeaver, 2015: Stationary waves (orographic and thermally forced). pp. 431-445 in *Encyclopedia of the Atmospheric Sciences, 2nd Edition*, *Volume 2*, ed. G. R. North, J. Pyle, and F. Zhang, Academic Press, 464 pp.

Palmen, E., and C. W. Newton, 1969: *Atmospheric Circulation Systems*. Academic Press, 603 pp. + xvii.

Rackow, T., D. V. Sein, T. Semmler, S. Danilov, N. V. Koldunov, D. Sidorenko, Q. Wang, and T. Jung, 2020: Sensitivity of deep ocean biases to horizontal resolution in prototype CMIP6 simulations with AWI-CM1.0. *Geosci. Model Dev*., **12**, 2635–2656, https://doi.org/10.5194/gmd-12-2635-2019.

Rind, D., R. Suozzo, N. K. Balachandran, A. Lacis, and G. Russell, 1988: The GISS global climate-middle atmosphere model. Part I: Model structure and climatology. *J. Atmos. Sci.*, **45**, 329-370, https://journals.ametsoc.org/toc/atsc/45/3.

Roberts, M. J., and 13 co-authors, 2019: Description of the resolution hierarchy of the global coupled HadGEM3-GC3.1 model as used in CMIP6 HighResMIP experiments, *Geosci. Model Dev.*, **12**, 4999-5028, 2019 https://doi.org/10.5194/gmd-12-4999-2019.

Rong, X., and 10 co-authors, 2019: The CAMS climate system model and a basic evaluation of its climatology and climate cariability simulation. *J. Meteorological Research*, **32**, 839-861, doi: 10.1007/s13351-018- 8058-x.

Simpson, I. R., Richard Seager, M. Ting, and T. A. Shaw, 2015: Causes of change in Northern Hemisphere winter meridional winds and regional hydroclimate, *Nature Climate Change*, **6**, 65-70, https://doi.org/10.1038/nclimate2783.

Smagorinsky, J., 1953: The dynamical influence of large-scale heat sources and sinks on the quasi-stationary mean motions of the stratosphere. *Quarterly Journal of the Royal Meteorological Society*, **79**, 342-366, https://doi.org/10.1002/qj.49707934103.

Swain, D. L., M. Tsiang, M. Haugen, D. Singh, A. Charland, B. Rajaratnam, and Noah S. Diffenbaugh, 2014: The extraordinary California drought of 2013/2014: Character, context, and the role of climate change. *Bull. Amer. Meteor. Soc.*, **95**, S3-S7, https://deeptis47.github.io/papers/Swain2014.pdf.

Swart, N. C., and 21 co-authors, 2019: The Canadian Earth System Model version 5 (CanESM5.0.3). *Geosci. Model Dev.*, https://doi.org/10.5194/gmd-2019-177.

Tatebe, H., and 25 co-authors, 2019: Description and basic evaluation of simulated mean state, internal variability, and climate sensitivity in MIROC6, *Geosci. Model Dev*., **12**, 2727-2765, https://doi.org/10.5194/gmd-12-2727-2019.

van Loon, H., and R. L. Jenne, 1972: The zonal harmonic standing waves in the southern hemisphere. *J. Geophys. Res. Oceans Atmos.*, **77**, 992-1003, https://doi.org/10.1029/JC077i006p00992.

van Loon, H., R. L. Jenne, and K. Labitzke, 1973: Zonal harmonic standing waves. *J. Geophys. Res. Oceans Atmos.*, **78**, 4463-4471, https://doi.org/10.1029/JC078i021p04463.

Wallace, J. M., and P. V. Hobbs, 2006: *Atmospheric Science: An Introductory Survey (2nd Edition)*, Academic Press, 483 pp.+xvi.

Wills, R. C. J., R. H. White, and X. L. Levine, 2019: Northern Hemisphere stationary waves in a changing climate. *Current Climate Change Reports*, **5**, 372-389, https://doi.org/10.1007/s40641-019-00147-6.

Wu, T., and 21 co-authors, 2019: The Beijing Climate Center Climate System Model (BCC-CSM): the main progress from CMIP5 to CMIP6. *Geosci. Model Dev*., **12**, 1573-1600, DOI:10.5194/gmd-12-1573-2019.

Yang, Y.-M., B. Wang, J. Cao, L. Ma, and J. Li, 2020: Improved historical simulation by enhancing moist physical parameterizations in the climate system model NESM3.0, *Climate Dynamics*, 54: 3819-3840, https://doi.org/10.1007/s00382-020-05209-2.

Yukimoto, S., and 16 co-authors, 2019: The Meteorological Research Institute Earth System Model Version 2.0, MRI-ESM2.0: Description and basic evaluation of the physical component, *J. Met. Soc. Japan*, **97,** 931-965, https://doi.org/10.2151/jmsj.2019-051.

TABLE 1. Data sources: reanalyses and climate models.

	Name	Source	Year	Atmosphere	#lev	Top	Horizontal Spacing	Reference
	ERA-Interim	ECMWF	2008	IFS Cy31r2	60	65 km	~80 km	Dee et al. (2011)
	JRA-55	JMA	2014	JMA 2009 NWP	60	65 km	~55 km	Kobayashi et al. (2015)
	ERA5	ECMWF	2018	IFS Cy41r2	137	80 km	~30 km	Hersbach et al. (2020)
	MERRA2	NASA GSFC	2017	GEOS-5	72	80 km	~50 km	Gelaro et al. (2017)
1	AWI-CM-1-1-MR	AWI	2018	ECHAM6.3.04p1	95	80 km	~150 km	Rackow et al. (2019)
2	BCC-CSM2-MR	BCC	2017	BCC_AGCM3_MR	46	45 km	~150 km	Wu et al. (2019)
3	CAMS-CSM1-0	CAMS	2016	ECHAM5_CAMS	31	30 km	~150 km	Rong et al. (2019)
4	CanESM5	CCCma	2019	CanAM5	49	50 km	~250 km	Swart et al. (2019)
5	CESM2	NCAR	2018	CAM6	32	40 km	~100 km	Danabasoglu et al. (2020))
6	CNRM-CM6-1	CNRM-CERFACS	2017	Arpege 6.3	91	80 km	~150 km	Brient et al. (2019)
7	E3SM-1-0	E3SM-Project	2018	EAM v1.0	72	65 km	~50 km	Golaz et al. (2019)
8	EC-Earth3	EC-Earth Consortium	2019	IFS cy36r4	91	80 km	~80 km	Massonnet et al. (2020)
9	GFDL-CM4	GFDL	2018	GFDL-AM4.0.1	33	50 km	~100 km	Held et al. (2019)
10	GISS-E2-1-G	NASA GISS	2019	GISS-E2.1	40	65 km	~250 km	Kelley et al. (2020)
11	HadGEM3-GC31-LL	MOHC / NERC	2016	MetUM-GA7.1	85	85 km	~250 km	Roberts et al. (2019)
12	IPSL-CM6A-LR	IPSL	2017	LMDZ	79	80 km	~250 km	Boucher et al. (2020)
13	MCM-UA-1-0	University of Arizona	1991*	GFDL R30	14	30 km	~350 km	Delworth et al. (2002)*
14	MIROC6	MIROC	2017	CCSR AGCM	81	85 km	~250 km	Tatebe et al. (2019)
15	MRI-ESM2-0	MRI	2017	MRI-AGCM3.5	80	80 km	~120 km	Yukimoto et al. (2019)
16	NESM3	NUIST	2016	ECHAM v6.3	47	80 km	~250 km	Yang et al. (2020)
17	NorCPM1	NCC	2019	CAM-OSLO4.1	26	45 km	~250 km	Guo et al. (2019)
18	SAM0-UNICON	SNU	2017	CAM5.3/UNICON	30	45 km	~120 km	Park et al. (2019)

* This model was built and frozen around 1991. Delworth et al. (2002) document various published versions of the model; this particular version is R30c in their Table 3 (R. J. Stouffer, personal communication, July 2020).

Reanalysis characteristics are from https://cera-www.dkrz.de/WDCC/ui/cerasearch and other online sources, accessed August 2020.

Climate model characteristics are from https://wcrp-cmip.github.io/CMIP6_CVs/docs/CMIP6_source_id.html and https://cera-www.dkrz.de/WDCC/ui/cerasearch/cmip6?input=CMIP6.CMIP.[institution].[modelname], accessed July 2020

TABLE 2. Amplitude and phase values of geopotential height Fourier components for January 1990-2013 climatological means.

⋯	45°N								45°S							
⋯	850 hPa Amplitude [m]				850 hPa Phase [λ, °E]				850 hPa Amplitude [m]				850 hPa Phase [λ, °E]			
Zonal Wave# :	1	2	3	4	1	2	3	4	1	2	3	4	1	2	3	4
ERA5	66.0	47.8	53.2	12.6	24.1	147.1	−27.2	−58.7	25.4	10.0	10.4	6.7	−142.0	120.3	−174.6	−76.7
CESM2	79.1	49.3	61.9	14.6	26.6	142.9	−17.7	−32.1	32.6	3.7	20.6	10.5	−127.2	148.8	−124.6	−66.3
GFDL−CM4	45.7	51.2	53.7	16.5	23.9	136.6	−36.4	−49.0	34.8	9.5	9.1	4.6	−138.1	94.1	−171.1	−45.2
GISS−E2−1−G	57.5	39.7	23.1	14.7	34.5	139.5	−30.2	16.8	19.4	6.7	3.4	11.6	−148.5	111.5	−157.0	−17.3
⋯	500 hPa Amplitude [m]				500 hPa Phase [λ, °E]				500 hPa Amplitude [m]				500 hPa Phase [λ, °E]			
Zonal Wave# :	1	2	3	4	1	2	3	4	1	2	3	4	1	2	3	4
ERA5	118.5	78.4	86.0	27.0	−16.2	96.2	−50.9	−72.1	41.2	11.6	23.1	13.2	−144.1	106.9	−175.0	−99.4
ERA−I	119.8	79.9	87.2	27.4	−15.8	97.8	−49.9	−71.9	40.8	11.4	22.7	13.2	−143.8	107.0	−174.9	−98.9
JRA−55	119.7	78.8	86.9	26.5	−16.5	95.9	−50.0	−72.5	41.0	11.5	22.5	13.5	−143.6	103.9	−173.1	−98.3
MERRA2	119.6	79.6	86.4	27.0	−16.4	97.6	−49.6	−69.3	41.6	12.6	22.5	12.9	−144.2	106.1	−173.2	−98.3
CESM2	130.6	67.2	91.8	22.1	−11.2	96.4	−41.3	−60.2	45.9	1.6	41.7	19.3	−130.9	−68.2	−133.9	−85.3
GFDL CM4	96.0	85.5	86.4	33.8	−25.8	90.2	−57.5	−76.1	49.2	13.1	18.6	9.9	−141.1	78.9	−169.8	−77.5
GISS−E2−1−G	106.3	59.7	40.3	20.1	2.3	92.9	−66.0	5.8	34.7	7.6	9.6	17.5	−153.3	108.3	177.9	−28.3
⋯	200 hPa Amplitude [m]				200 hPa Phase [λ, °E]				200 hPa Amplitude [m]				200 hPa Phase [λ, °E]			
ERA5	170.0	96.4	100.3	30.9	−45.8	71.0	−62.6	−83.9	48.7	18.7	28.0	19.8	−156.2	93.3	−177.9	−104.9
ERA−I	170.4	96.4	100.2	31.5	−45.3	72.4	−62.1	−85.1	48.3	18.8	27.3	19.5	−156.7	94.5	−177.7	−104.6
JRA−55	169.9	97.2	100.9	30.8	−45.3	71.2	−62.6	−85.1	48.7	18.6	27.4	19.3	−155.3	91.7	−177.2	−104.1
MERRA2	172.6	97.4	101.2	31.3	−46.0	72.2	−61.8	−83.5	49.1	19.2	27.8	19.7	−156.1	93.2	−176.1	−105.1
CESM2	165.4	74.5	101.3	25.4	−33.2	74.0	−47.0	−66.9	49.6	6.8	56.3	27.6	−144.2	−35.5	−139.6	−91.2
GFDL CM4	138.5	98.2	94.6	37.7	−52.9	70.9	−61.7	−92.5	58.5	20.0	23.1	15.5	−151.6	72.9	−174.9	−88.8
GISS−E2−1−G	149.2	78.6	51.3	17.8	−23.8	69.0	−84.9	5.4	46.7	11.7	12.8	26.2	−175.2	79.6	176.0	−37.3

TABLE 3. Amplitude and phase values of geopotential height Fourier components for July 1990-2013 climatological means.*

⋯	45°N								45°S							
⋯	850 hPa Amplitude [m]				850 hPa Phase [λ, °E]				850 hPa Amplitude [m]				850 hPa Phase [λ, °E]			
Zonal Wave‡‡ :	1	2	3	4	1	2	3	4	1	2	3	4	1	2	3	4
ERA5	43.3	29.4	11.8	4.5	−71.6	32.3	−102.3	−167.1	15.4	9.2	27.9	6.3	−116.9	−1.5	122.2	−131.0
CESM2	0	0	0	0	0	0	0	0	26.2	25.2	33.3	10.2	−79.8	28.2	168.4	−135.1
GFDL−CM4	34.5	30.4	7.7	4.3	−72.2	35.0	−94.6	−144.1	25.0	13.6	31.9	12.8	−64.2	37.0	−166.4	−134.7
GISS−E2−1−G	36.4	25.2	8.4	4.8	−63.8	48.1	−86.8	−136.6	4.6	10.6	36.1	3.8	−157.8	−5.4	120.8	−114.3
⋯	500 hPa Amplitude [m]				500 hPa Phase [λ, °E]				500 hPa Amplitude [m]				500 hPa Phase [λ, °E]			
Zonal Wave‡‡ :	1	2	3	4	1	2	3	4	1	2	3	4	1	2	3	4
ERA5	26.6	11.8	10.4	7.3	−64.5	94.0	−49.0	−86.1	19.8	7.4	37.8	9.2	−131.2	17.0	116.6	−136.6
ERA−I	26.8	12.3	11.1	7.3	−63.3	95.7	−46.8	−85.3	20.1	7.4	37.7	9.0	−130.8	17.1	115.9	−134.8
JRA−55	24.5	11.8	11.6	7.0	−60.3	95.9	−47.3	−83.3	20.8	7.3	37.3	9.5	−130.5	17.4	115.4	−133.6
MERRA2	27.2	13.1	12.2	7.0	−67.2	91.4	−46.3	−87.1	19.6	9.2	36.5	9.0	−131.0	18.2	117.0	−135.7
CESM2	40.7	8.0	5.9	11.7	−87.7	5.8	−83.0	−69.6	33.3	33.6	46.6	16.3	−73.5	36.9	166.1	−146.9
GFDL CM4	13.6	10.1	4.4	8.3	−44.1	121.5	−20.6	−60.2	28.8	11.7	46.7	18.0	−54.7	55.7	−169.5	−136.3
GISS−E2−1−G	22.6	29.2	14.5	13.6	−19.5	129.1	−25.4	−43.3	14.6	6.5	51.6	4.5	168.8	43.6	114.0	−119.0
⋯	200 hPa Amplitude [m]				200 hPa Phase [λ, °E]				200 hPa Amplitude [m]				200 hPa Phase [λ, °E]			
ERA5	5.4	24.0	5.0	14.5	85.5	−169.0	123.0	−111.4	23.0	14.2	40.6	11.8	−95.3	105.7	106.9	−126.7
ERA−I	5.8	24.7	5.4	15.1	75.7	−169.9	123.1	−113.1	22.5	14.6	40.5	11.5	−95.3	107.5	106.0	−126.2
JRA−55	8.8	24.3	4.3	14.9	84.8	−170.3	118.6	−113.0	24.5	14.7	39.6	12.0	−95.0	107.1	105.9	−125.4
MERRA2	5.4	23.6	4.5	15.1	102.4	−168.1	112.9	−114.2	23.3	13.9	39.8	12.0	−93.3	100.6	107.1	−125.5
CESM2	18.8	31.6	18.4	18.6	164.0	−128.5	92.2	−92.9	43.2	35.2	54.6	20.3	−63.9	50.1	166.9	−147.4
GFDL CM4	21.1	29.8	13.0	11.8	113.7	−147.9	116.4	−95.8	45.7	14.1	53.1	20.8	−46.2	120.6	−166.3	−137.0
GISS−E2−1−G	27.3	43.2	14.5	24.9	88.5	171.4	−50.8	−28.1	6.8	18.9	63.2	4.6	90.7	117.4	108.7	−100.8

* Zero value flags MISSING DATA.

SUPPLEMENTARY MATERIAL

1. Variance fractions

From Equation (3), the cumulative fraction of total variance contributed by wavenumbers 1 through N is $\left[\frac{1}{2}\sum_{n=1}^{N}({a_n}^2 + {b_n}^2) \right] \Big/ \left[(2\pi)^{-1} \int_0^{2\pi}[f(\lambda) - C_0]^2 \, d\lambda \right]$. Contour maps of this quantity are shown for ERA5 reanalysis in Figure S1 for $N = 2, 3, \text{and } 4$. At nearly all latitudes and altitudes, more than 80% of the variance in is captured by the first three or four wavenumbers. The only exceptions are near the surface (where tropography makes the geopotential field less smooth) and around 45°N and 1-2 scale heights during the month of July, where a fair amount of wavenumber 1-3 activity occurs in both models and observations (see Fig. 8 in the main text). But even wavenumbers 1-5 include less than 80% of total variance at ~45°N and 1 scale height, so this one location in latitude / altitude space is incompletely represented by our Fourier analysis.

Integrating the fields shown in Figure S1 vertically (and weighting by pressure, i.e. by the mass of each layer) gives the line plots in Figure S2. From this perspective, just the first two Fourier wavenumbers are needed to encompass more than half the total variance, and including wavenumbers up to and including 4 gives more than 80% at all latitudes and more than 90% at most latitudes.

2. Uncertainty due to initial conditions

Two of the three climate models appearing in Figures 6-9 of the main text—CESM2 and GISS-E2-1-G—provided to CMIP6 an ensemble of historical runs differing only by slight variations in their initial conditions. Figure S3 plots Fourier amplitude and phase at the 500 hPa pressure level from 10 ensemble members of each of model. Figure S4 plots analogous data from the 500 hPa pressure level. The two figures also include data from the four reanalysis projects studied in the main text. By selecting a single pressure level, each figure element can show line plots from an unlimited number of data sources, as in Figs. 10-13 in the main text.

The reanalysis results plot virtually on top of each other (as noted in the main text). Different ensemble members from either of the two models exhibit a wider but still limited spread. At many latitudes, results from all reanalyses and from both models overlap, suggesting no significant disagreement in the first three Fourier components. At other latitudes, the ensembles separate cleanly from each other and/or from the reanalyses. For example, in all datasets January's peak amplitude occurs in Northern Hemisphere midlatitudes, but for wavenumber 3 the peak amplitudes from all GISS-E2-1-G ensemble members are less than values from all CESM2 ensemble members as well as reanalysis. This result implies that the GISS underestimates noted in the main text are robust to variations of the initial conditions.

Peixoto & Oort,
"Physics of Climate"

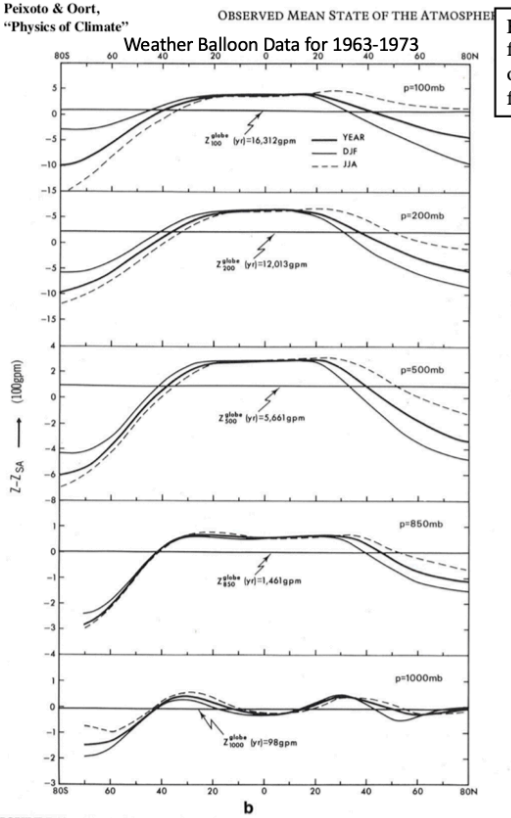

FIGURE 7.10. ~~(a) Meridional profiles of the zonal mean pressure (in mb) at various heights between 0.1 and 16 km.~~ (b) Meridional profiles of the zonal mean height (in units of 100 gpm ≃ 100 m) for various pressure levels between 1000 and 100 mb.

FIG. 1. Zonal mean geopotential height from (left) direct weather balloon observations and (right) JRA-55 reanalysis for the 1960s.

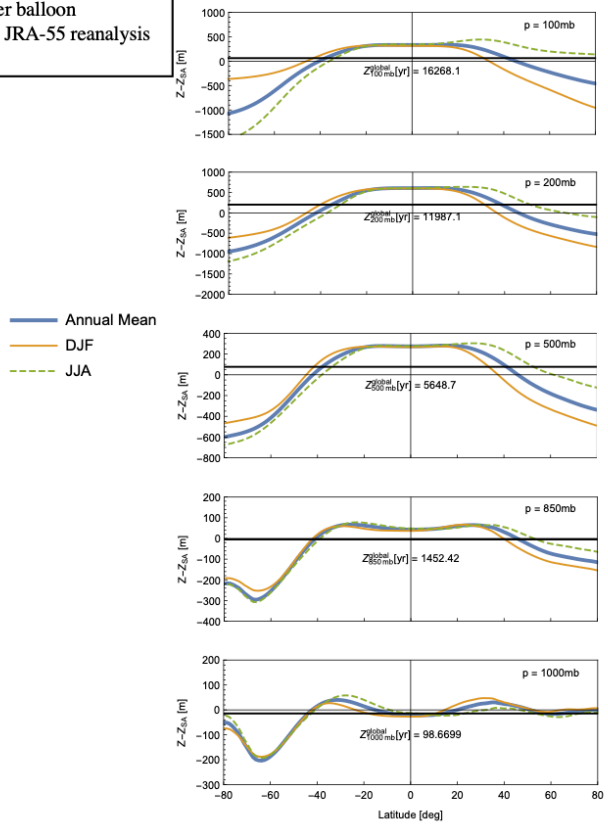

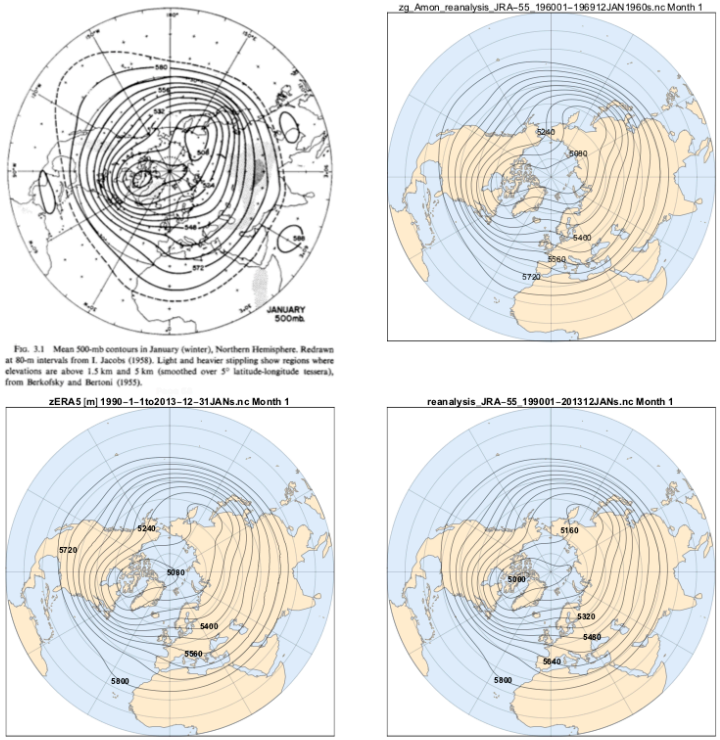

FIG. 3.1 Mean 500-mb contours in January (winter), Northern Hemisphere. Redrawn at 80-m intervals from I. Jacobs (1958). Light and heavier stippling show regions where elevations are above 1.5 km and 5 km (smoothed over 5° latitude-longitude tessera), from Berkofsky and Bertoni (1955).

FIG. 2. January Northern Hemisphere 500-hPa geopotential heights from (upper left) direct weather balloon observations, (upper right) JRA-55 reanalysis for the 1960s, (lower right) JRA-55 reanalysis for 1990-2013, and (lower left) JRA-55 reanalysis for 1990-2013.

Northern Hemisphere 500-mb Heights: Original vs Modern Reanalysis Climatology for July

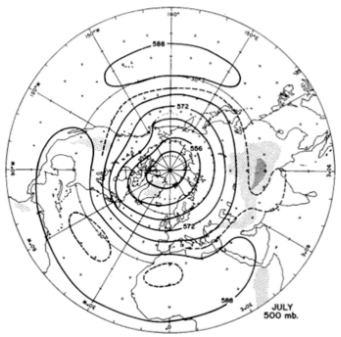

FIG. 3.2 Mean 500-mb contours in July (summer), Northern Hemisphere. (Redrawn, from I. Jacobs, 1958.)

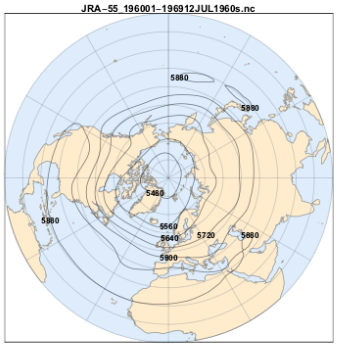

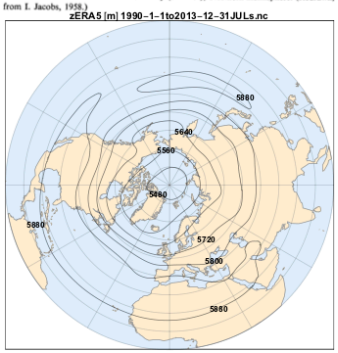

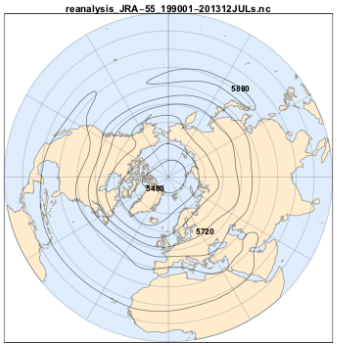

FIG. 3. As in Fig. 2 for July.

Southern Hemisphere 500-mb Heights: Original vs Modern Reanalysis Climatology for January

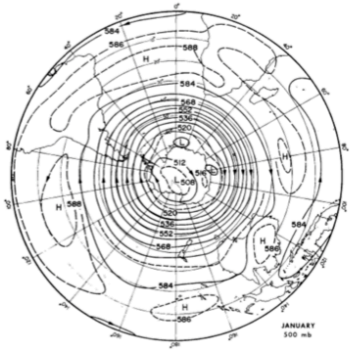

FIG. 3.3 Mean 500-mb contours (80-m interval) in January (summer), Southern Hemisphere. (After Taljaard *et al.*, 1969.)

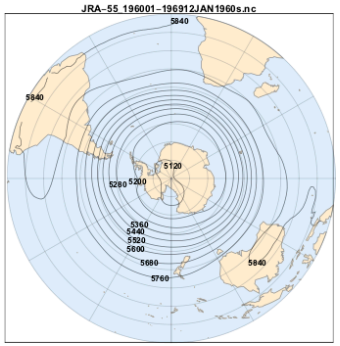

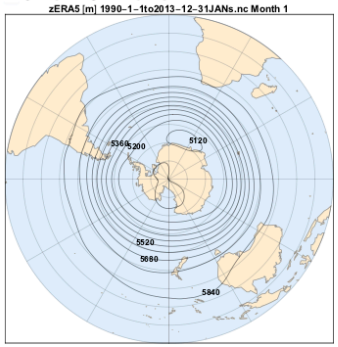

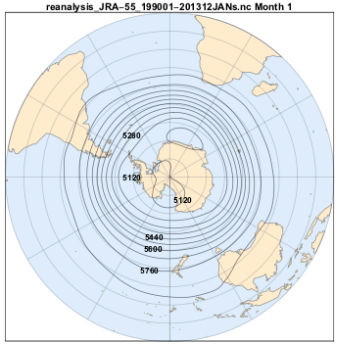

FIG. 4. As in Fig. 1 for January Southern Hemisphere.

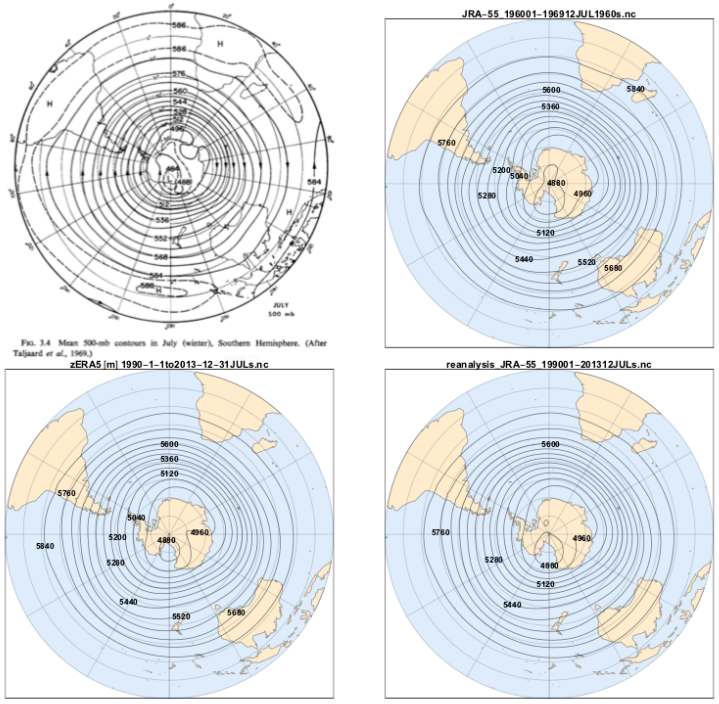

FIG. 3.4 Mean 500-mb contours in July (winter), Southern Hemisphere. (After Taljaard *et al.*, 1969.)

FIG. 5. As in Fig. 1 for July Southern Hemisphere.

Fourier Zonal Wave Amplitude: January

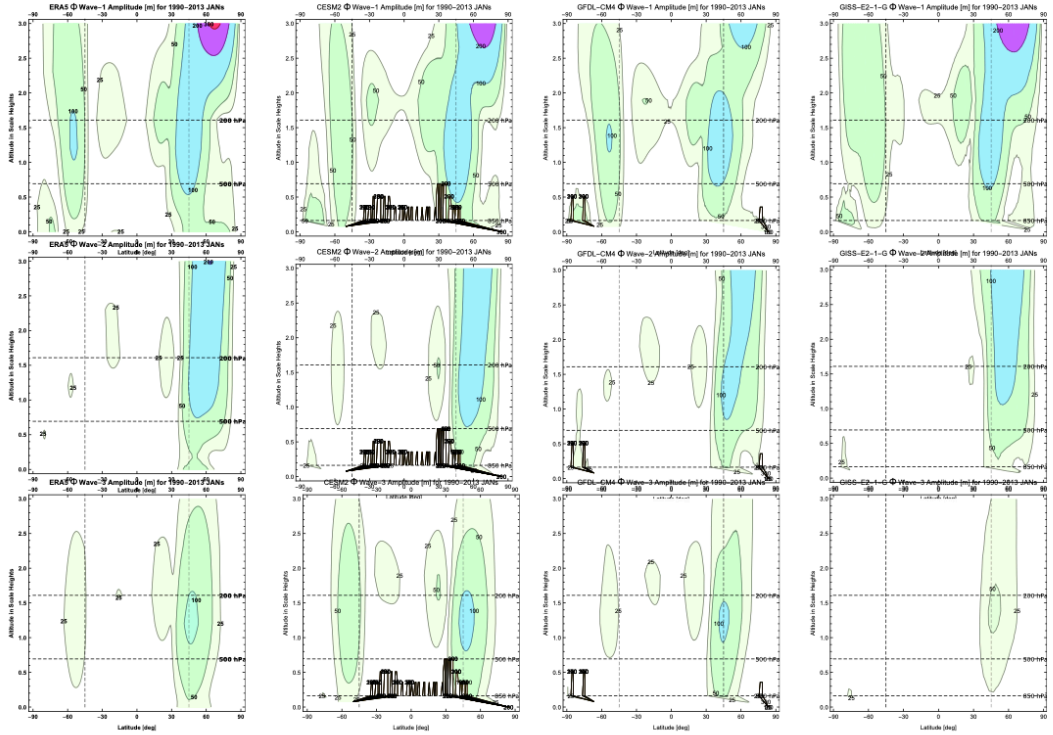

FIG. 6. January geopotential height amplitudes from (left column) reanalysis and (other columns) a selection of CMIP6 climate models. Rows 1-3 show results for Fourier zonal waves 1-3, respectively.

Fourier Zonal Wave Phase: January

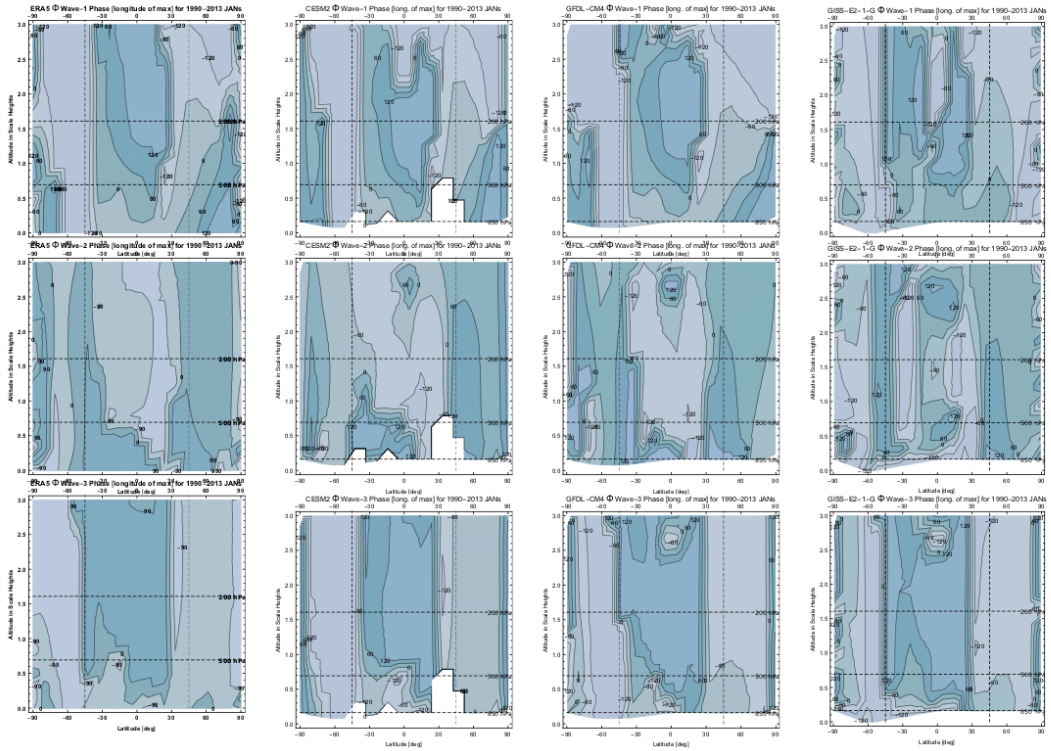

FIG. 7. As in Fig. 6 for wave phase (longitude of the first ridge, looking eastward from 0° longitude).

Fourier Zonal Wave Amplitude: July

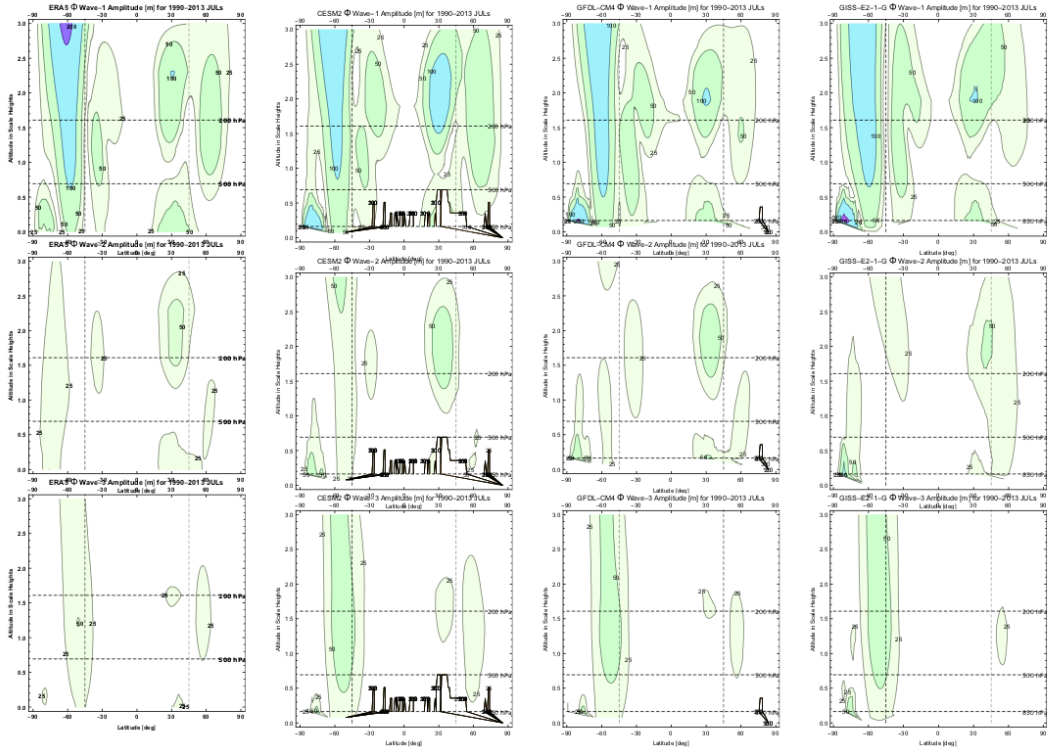

FIG. 8. As in Fig. 6 for July wave amplitude.

Fourier Zonal Wave Phase: July

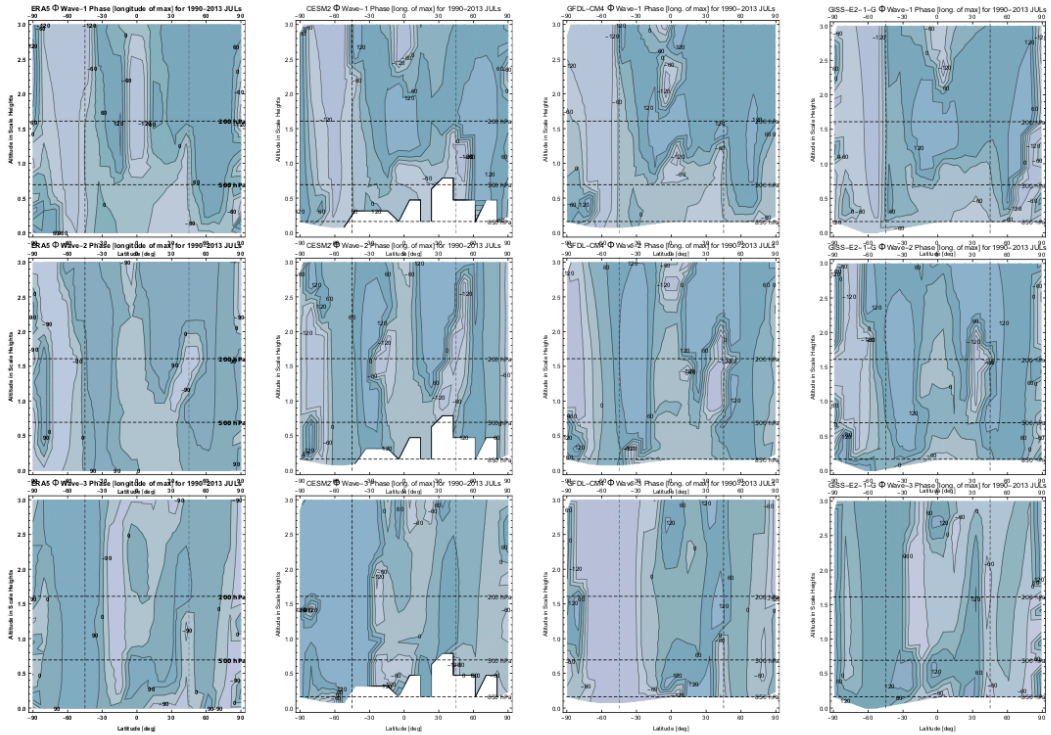

FIG. 9. As in Fig. 7 for July wave phase.

Fourier Zonal Wave Amplitude at Selected Levels: January

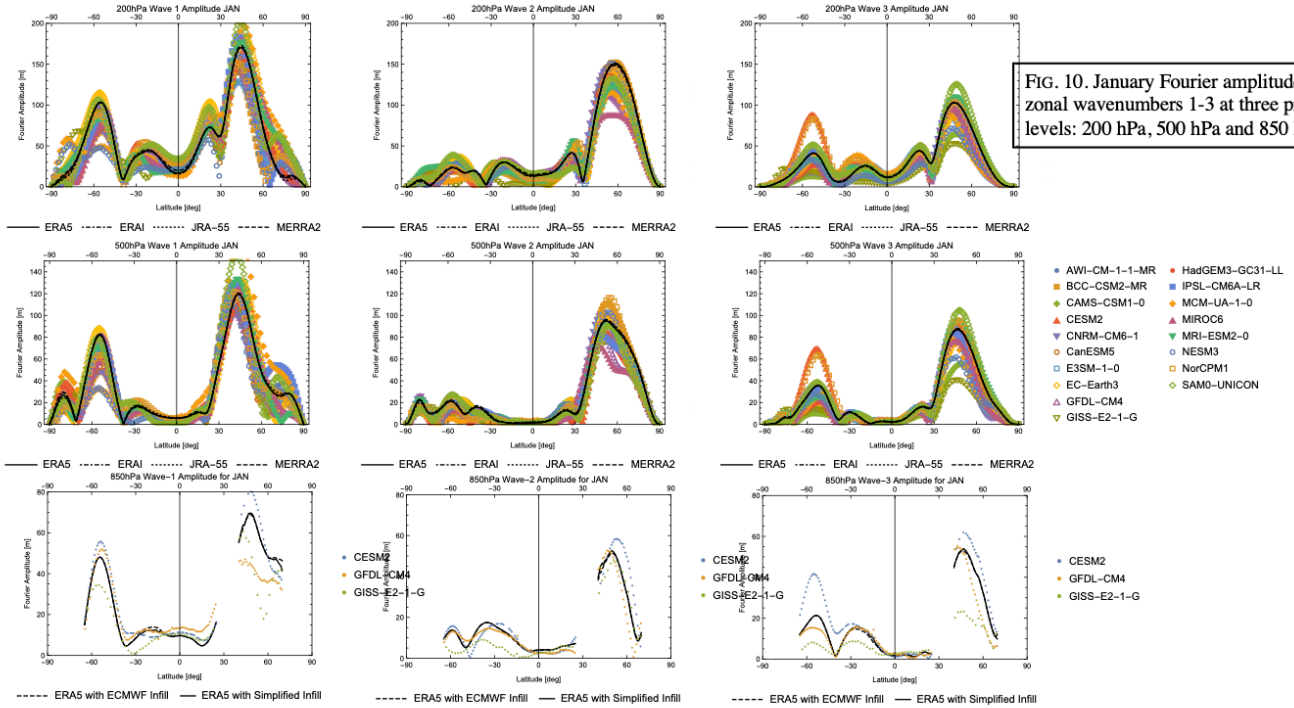

FIG. 10. January Fourier amplitudes for zonal wavenumbers 1-3 at three pressure levels: 200 hPa, 500 hPa and 850 hPa.

Fourier Zonal Wave Phase at Selected Levels: January

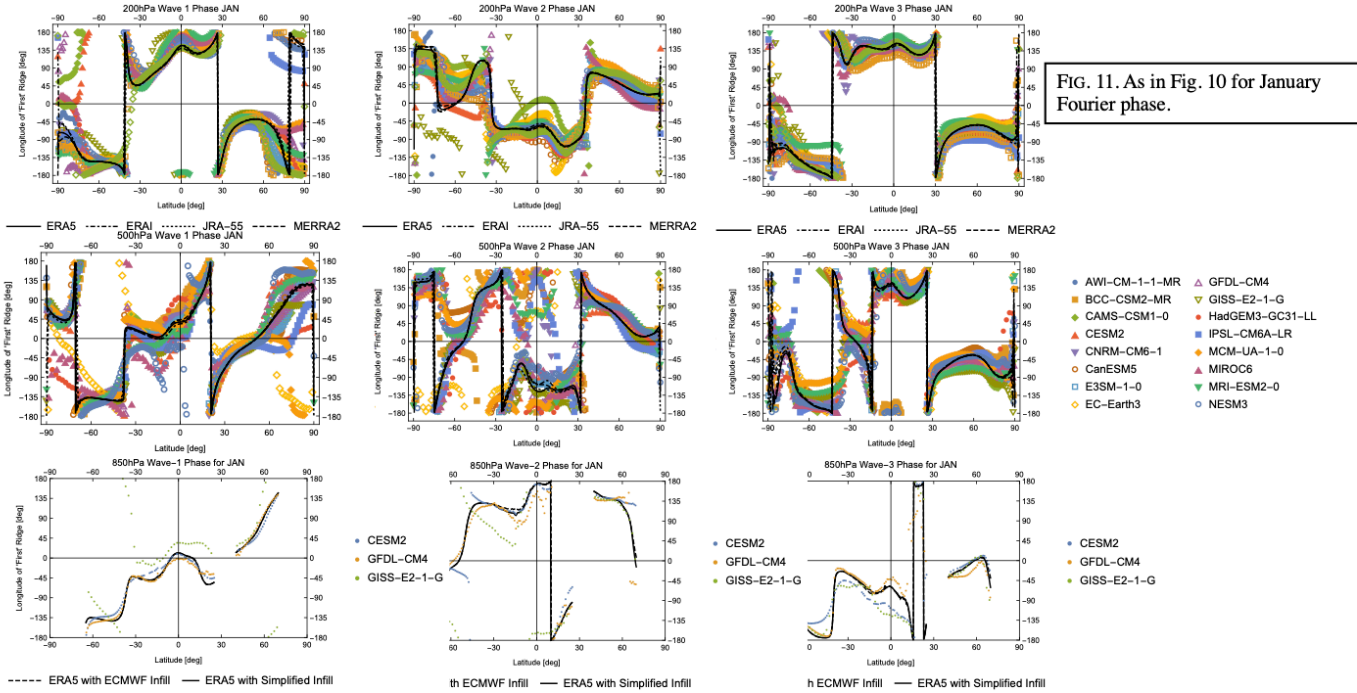

FIG. 11. As in Fig. 10 for January Fourier phase.

Fourier Zonal Wave Amplitude at Selected Levels: July

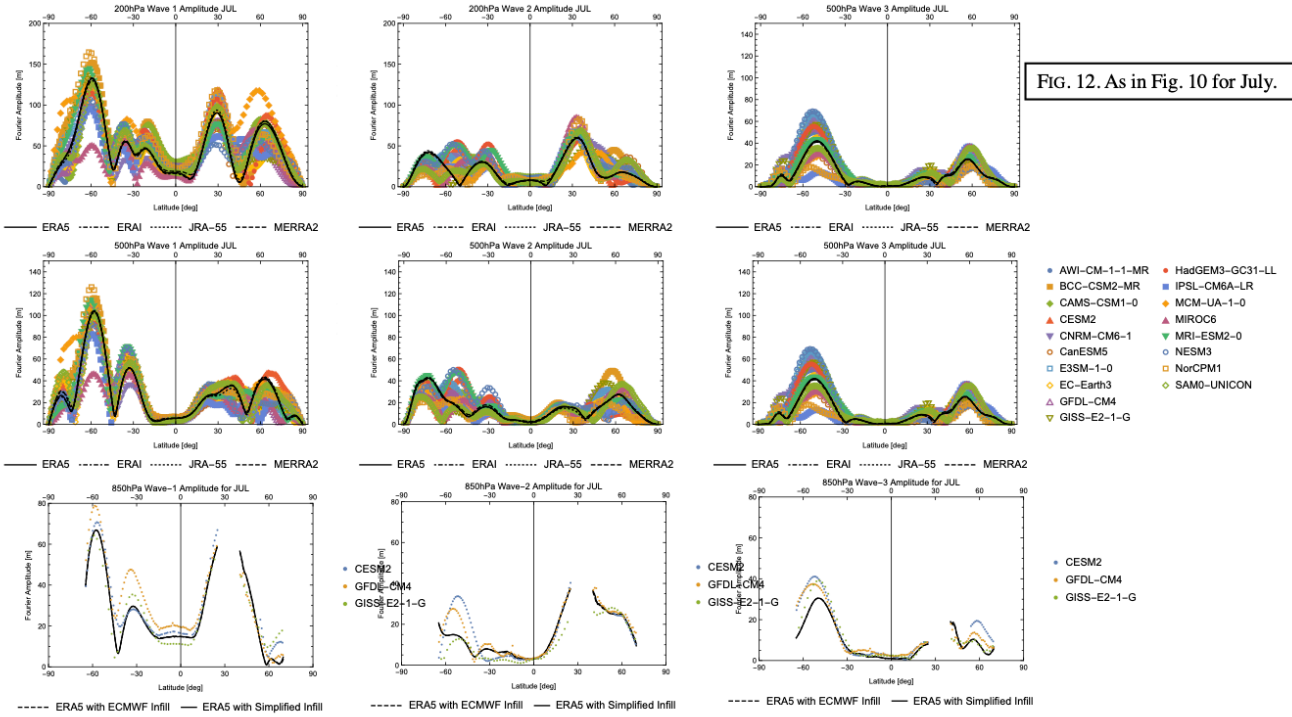

FIG. 12. As in Fig. 10 for July.

Fourier Zonal Wave Phase at Selected Levels: July

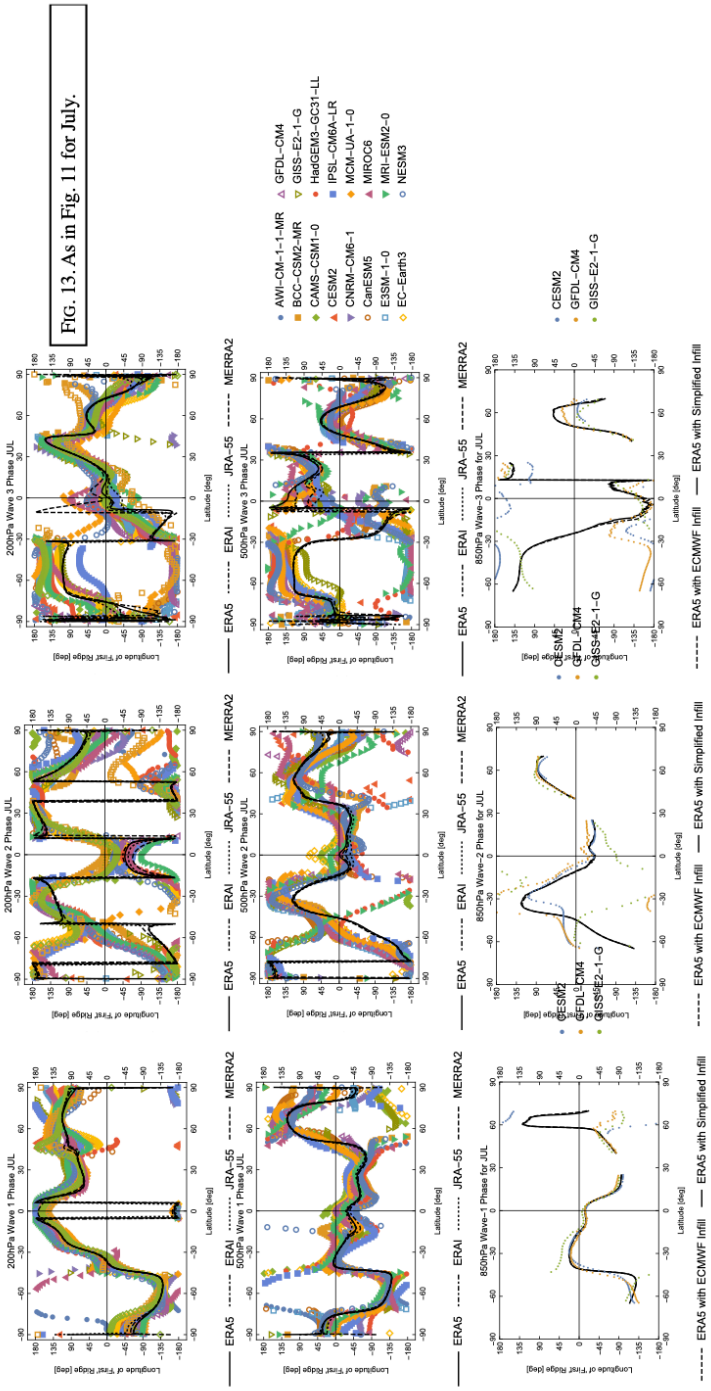

FIG. 13. As in Fig. 11 for July.

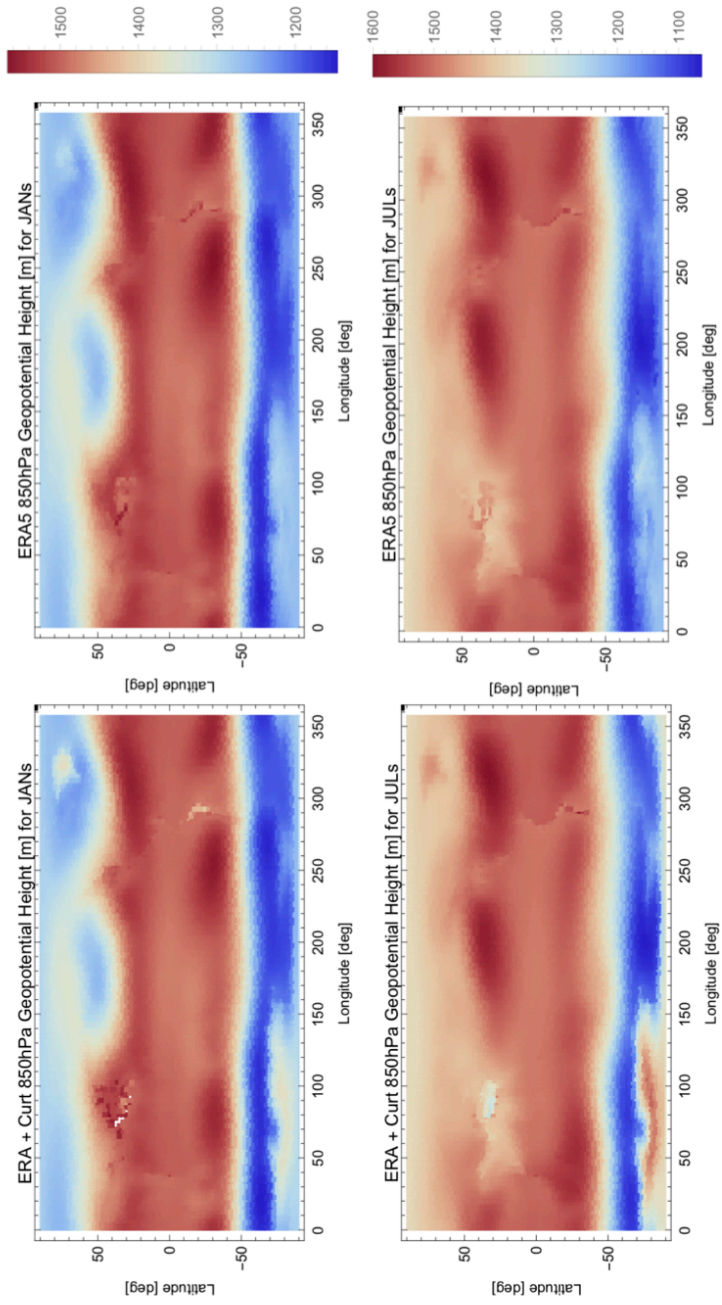

FIG. A1. Geopotential height field at 850 hPa in ERA5 data with the present study's infilling of below-surface values (left column) and with the original ECMWF infilling of below-surface values (right column) for January (top row) and July (bottom row) climatology.

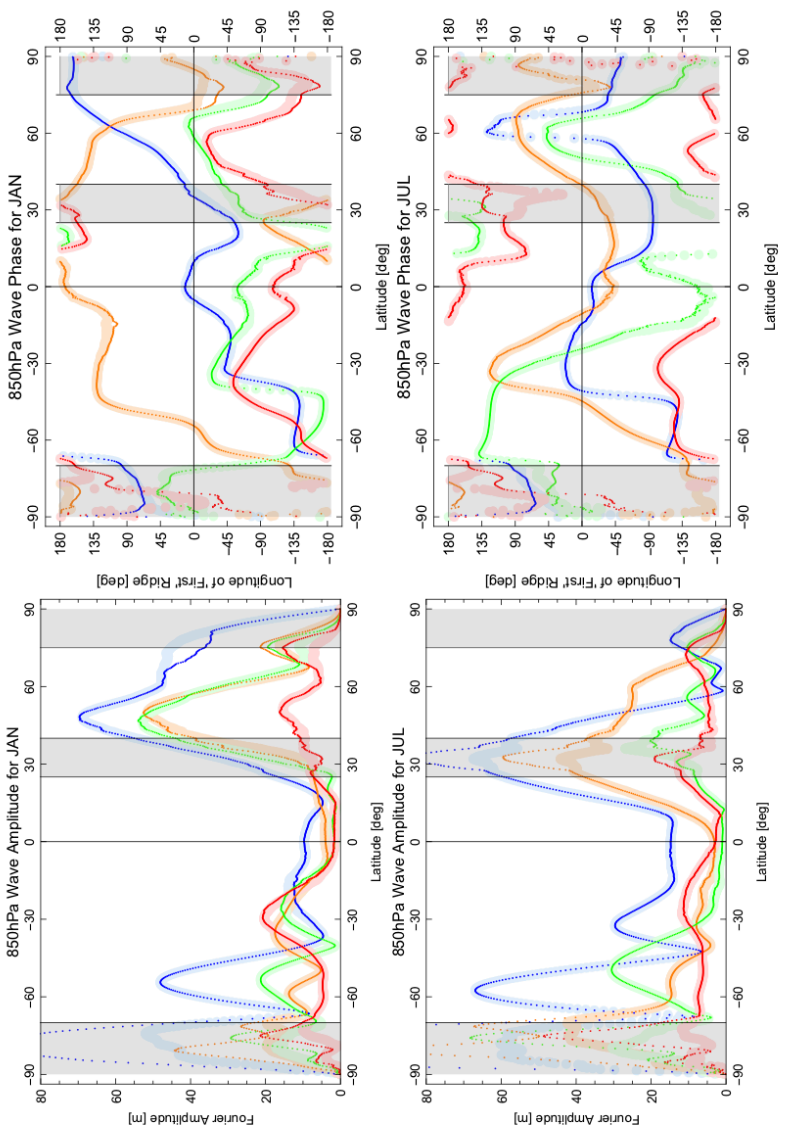

FIG. A2. Fourier amplitudes (left column) and phases (right column) of geopotential height field at 850 hPa for January (top row) and July (bottom row) climatology. The first 4 zonal wavenumbers are color-coded as indicated. Original ERA5 data appears in lighter colors; data with the present study's infilling of below-surface values appears in darker colors.

Figure S1: ERA5 Cumulative Fraction of Total Variance from Wavenumbers 1 to . . .

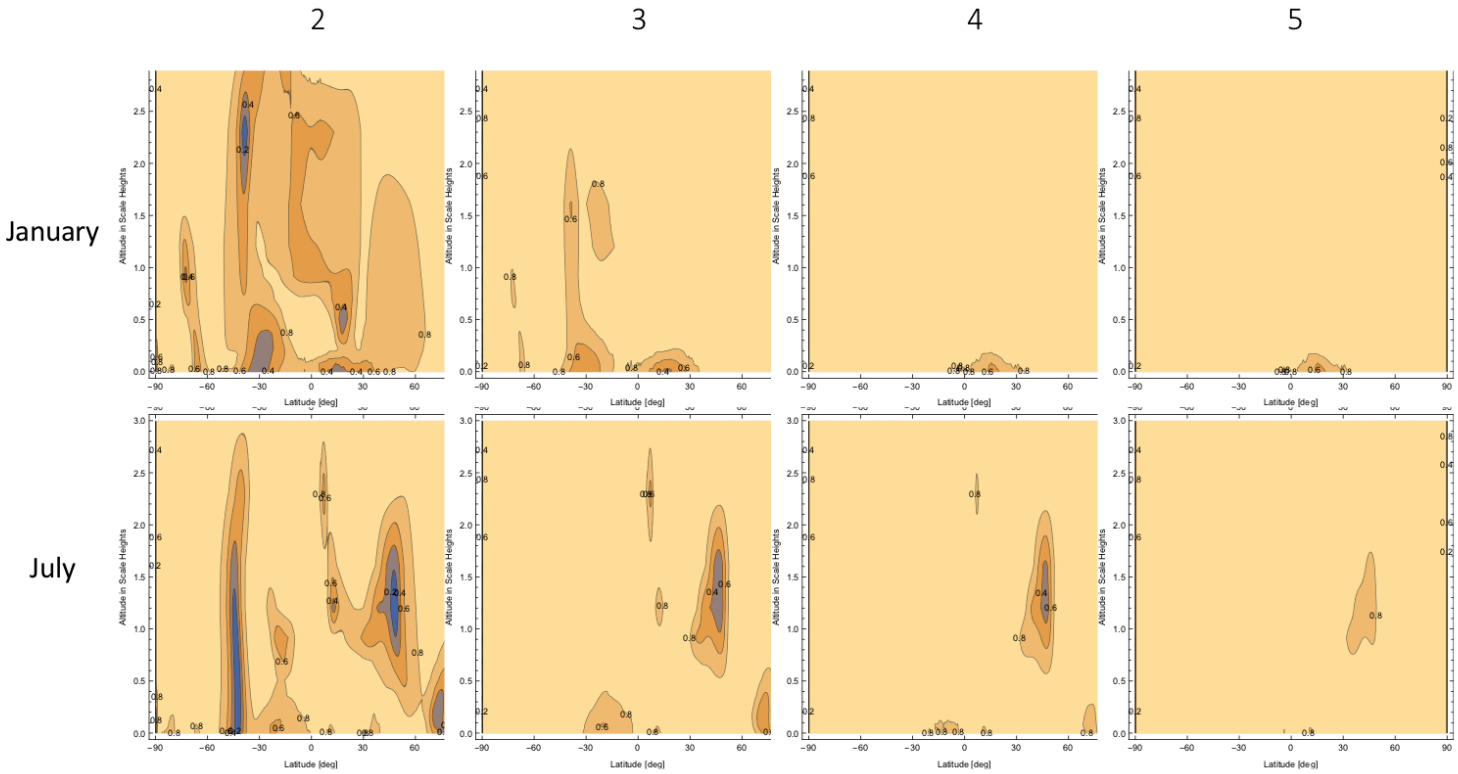

Figure S2

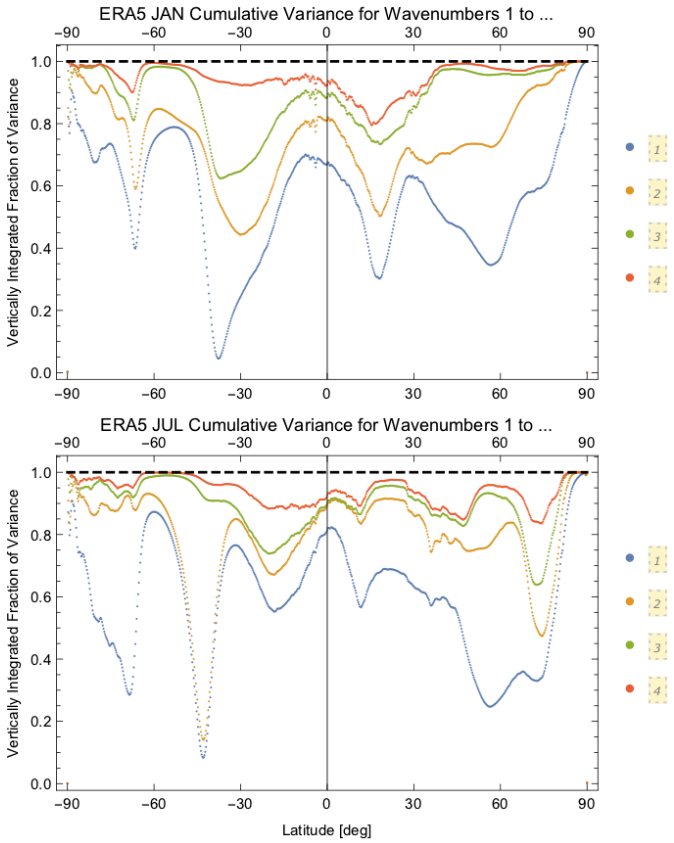
ERA5 JAN Cumulative Variance for Wavenumbers 1 to ...
ERA5 JUL Cumulative Variance for Wavenumbers 1 to ...
Vertically Integrated Fraction of Variance
Latitude [deg]
−90
−60
−30
0
30
60
90
0.0
0.2
0.4
0.6
0.8
1.0
1
2
3
4

Fig. S3: Fourier Components of CESM2 and GISS-E2-1-G Ensemble Runs at 500 hPa

January *July*

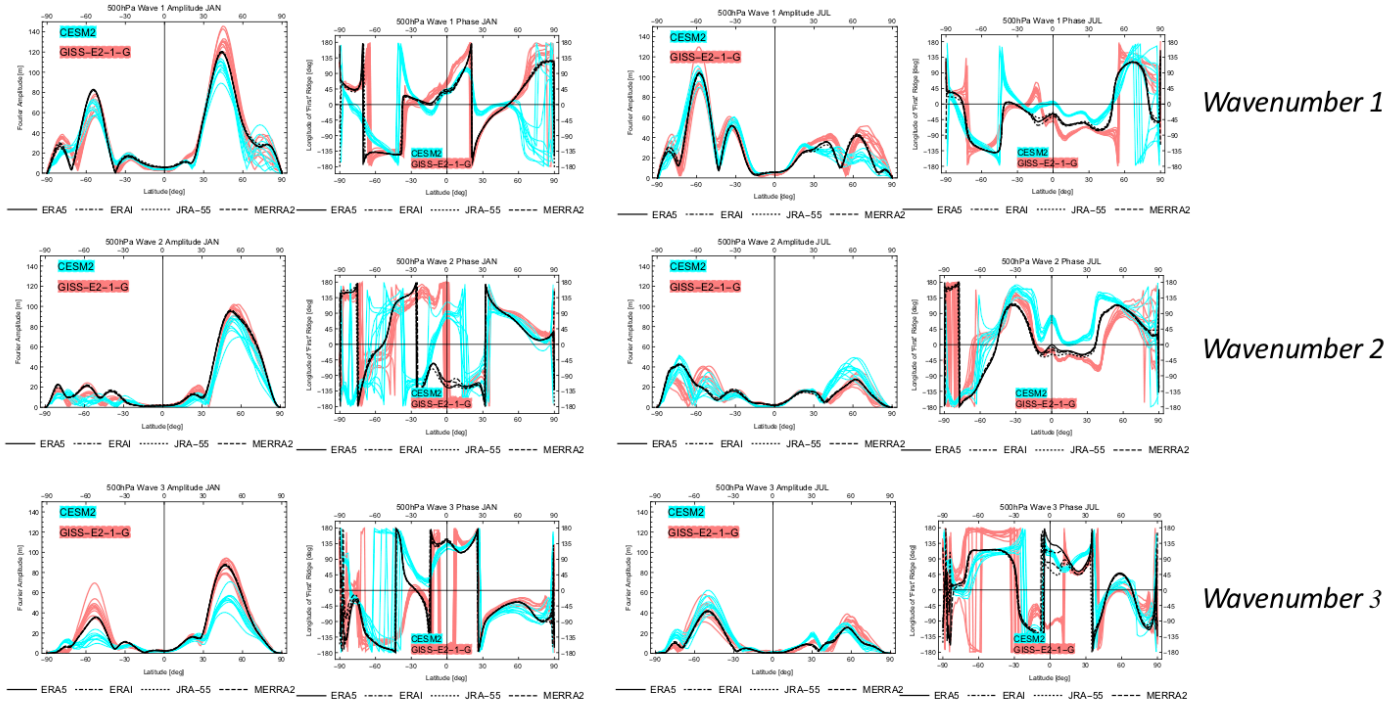

Wavenumber 1

Wavenumber 2

Wavenumber 3

Fig. S4: Fourier Components of CESM2 and GISS-E2-1-G Ensemble Runs at 200 hPa

January *July*

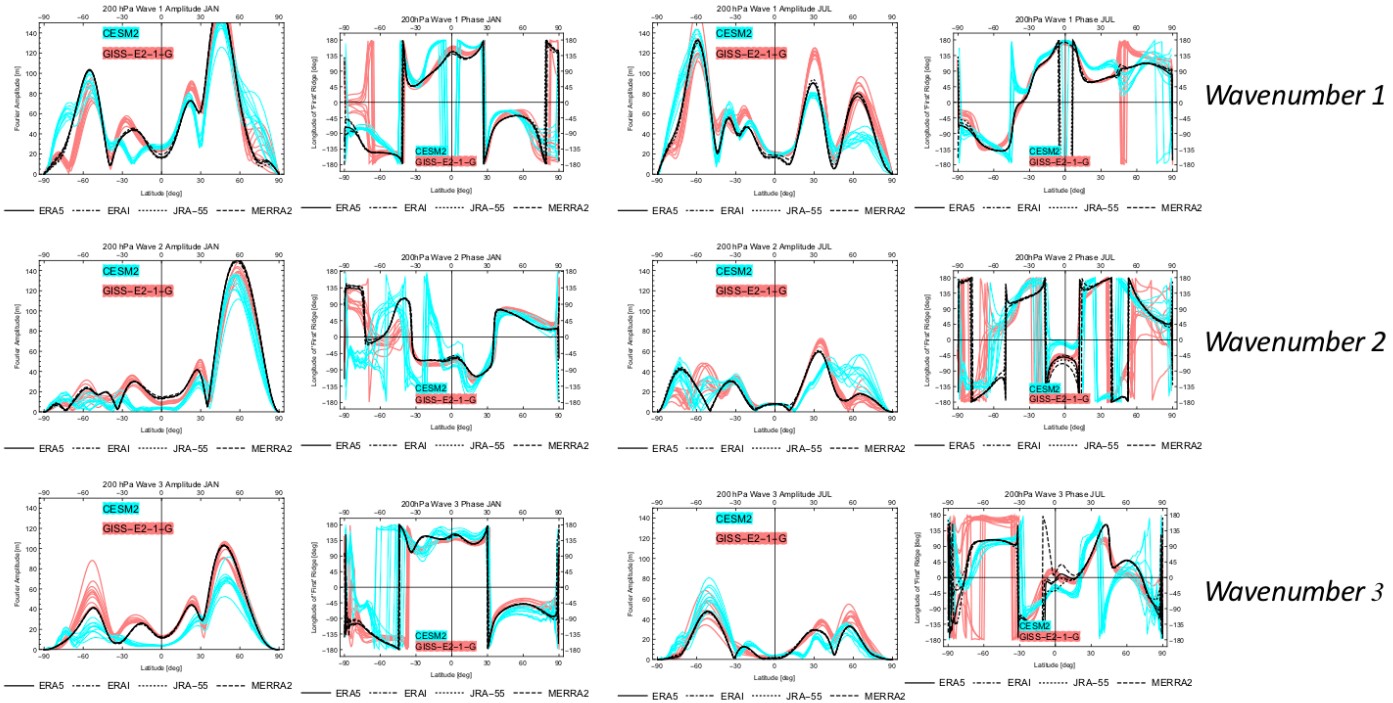

Wavenumber 1

Wavenumber 2

Wavenumber 3